Streaky perturbations in swept-wing flow over forward-facing step

Casacuberta, Jordi; Westerbeek, Sven; Franco, Juan Alberto; Groot, Koen J.; Hickel, Stefan; Hein, Stefan; Kotsonis, Marios

DOI
10.1103/PhysRevFluids.10.023902

Publication date
2025

Document Version
Final published version

Published in
Physical Review Fluids

Citation (APA)
Casacuberta, J., Westerbeek, S., Franco, J. A., Groot, K. J., Hickel, S., Hein, S., & Kotsonis, M. (2025). Streaky perturbations in swept-wing flow over forward-facing step. *Physical Review Fluids*, *10*(2), Article 023902. https://doi.org/10.1103/PhysRevFluids.10.023902

Streaky perturbations in swept-wing flow over forward-facing step

Jordi Casacuberta,[1] Sven Westerbeek,[1] Juan Alberto Franco,[2,3] Koen J. Groot,[4] Stefan Hickel,[1] Stefan Hein,[2] and Marios Kotsonis[1]

[1]*Department of Flow Physics and Technology, Faculty of Aerospace Engineering, Delft University of Technology, Kluyverweg 1, 2629HS Delft, The Netherlands*

[2]*Institute of Aerodynamics and Flow Technology, German Aerospace Center, Bunsenstrasse 10, 37073 Göttingen, Germany*

[3]*Universidad Politécnica de Madrid, Plaza Cardenal Cisneros 3, E-28040 Madrid, Spain*

[4]*Department of Mechanical Engineering, University of Wyoming, Laramie, Wyoming 82072, USA*

(Received 19 August 2024; accepted 10 January 2025; published 14 February 2025)

Stationary velocity-perturbation streaks have recently been identified in laminar swept-wing boundary-layer flow interacting with a surface forward-facing step. Streaky structures at the step promote early laminar-turbulent transition under certain conditions. This work utilizes direct numerical simulations to explore the mechanisms of growth of stationary streaks at the step and provides insight into their origin, nature, and spatial organization. The analysis is mainly focused on, but not restricted to, incoming perturbations in the form of stationary crossflow instability. Stationary streaky structures are found to be universal to swept forward-facing-step flow subjected to three-dimensional perturbations in the incoming boundary layer. The streaks at the step are primarily ascribed to the lift-up effect. They appear as a linear perturbation response of the highly sheared step flow to the cross-stream pattern of incoming perturbations. A mechanism of base-flow deceleration additionally contributes to feeding growth to the streaks. Linear stability analysis carried out through the harmonic Navier-Stokes method confirms that the streaks are a linear perturbation phenomenon. Effects of spanwise perturbation wavelength and effective sweep angle on the mechanisms of the streaks are also assessed.

DOI: 10.1103/PhysRevFluids.10.023902

I. INTRODUCTION

A novel flow structure has recently been reported in laminar swept-wing boundary-layer flow over a forward-facing step [1,2], which consists of stationary alternating regions of velocity excess and deficit that are distributed along the step edge. These stationary velocity-perturbation streaks develop spatially very close to the wall and form as a by-product of the interaction between the step geometry and three-dimensional perturbations in the incoming boundary layer. The identification of this flow feature in a structural sense reconciles with previous numerical and experimental studies reporting significant stationary-perturbation amplification around the upper step corner [3–5]. The perturbation streaks are found to play a key role in premature laminar-turbulent transition of swept-wing boundary-layer flow under interaction with surface steps [6]. Nonetheless, the flow mechanism giving rise to the streaks, as well as the nature and organization of this instability feature, remain largely unexplored. This work investigates the mechanisms responsible for the formation of stationary streaky structures in swept forward-facing-step flow.

A. Interaction between crossflow instability and forward-facing step

The main scope of this work is specifically placed on low-subsonic swept-wing boundary-layer flow. In low-disturbance environments, as in free flight, the amplification of stationary crossflow instability [7,8] predominantly drives the process of laminar-turbulent transition [9]. The reader is referred to Deyhle and Bippes [10] for a discussion on the complex process of receptivity, which eventually leads to the dominance of stationary (i.e., of zero temporal frequency) over traveling (i.e., of nonzero temporal frequency) crossflow instabilities. Notwithstanding the outcome of receptivity, the crossflow instability (CFI) itself is an intrinsic feature of three-dimensional swept-wing boundary layers. It is a modal instability of inviscid type associated to the existence of an inflectional velocity profile, the so-called crossflow profile, that arises from the combination of sweep angle and chordwise pressure gradient. In its stationary form, CFI appears as a wavelike velocity perturbation of null temporal frequency whose wavefronts are aligned approximately with the local direction of the inviscid streamlines far from the wall.

In the developed flow, i.e., the superposition of the laminar (unperturbed) base flow and perturbation fields, the spatial amplification of stationary CFI manifests as corotating vortices. These are referred to as the stationary crossflow vortices. Due to their stationary nature, the crossflow vortices have a large impact on the topology of the boundary layer. Namely, they displace low-momentum regions away from the wall and high-momentum regions towards the wall, therefore producing a strongly modulated base flow with strong spanwise and wall-normal shear regions. The subsequent growth of unsteady secondary instabilities supported by the localized shears in the modulated boundary layer typically leads the process of laminar breakdown [11–14]. An exhaustive review of experimental work on crossflow-dominated transitional flows can be found in Bippes [15].

While receptivity, growth, and breakdown of crossflow vortices over smooth idealized surfaces is now well understood, the presence of surface irregularities brings forth new challenges. The presence of steps on *realistic* engineering surfaces may alter the aforementioned classic transition route and shift the transition front upstream. The need to define manufacturing tolerances to minimize the impact of such steps in premature laminar-turbulent transition motivated a series of experimental and numerical studies in recent years [2–5,16]. Their main focus was placed on the characterization of interaction mechanisms between incoming (i.e., preexisting) stationary CFI and a forward-facing step. From the wealth of newly discovered step-flow features, significant debate has been generated on the origin of novel stationary-perturbation amplification detected at the step apex [2–5,16], between the wall and the incoming CFI passing above. Such novel stationary-perturbation amplification was first quantified as an additional peak in the *perturbation shape* (i.e., the perturbation profile along the wall-normal direction).

Tufts *et al.* [3] ascribe this novel peak in the perturbation shape to the *interaction* between a confined region of recirculating flow on the upper wall of the step and the incoming crossflow vortices. However, the validity of the model of Tufts *et al.* [3] has been questioned [1,2,4,17]. On the one hand, the near-wall stationary-perturbation amplification identified by Tufts *et al.* [3] is linked to CFI destabilization by inflectional profiles of the distorted step flow [4]. On the other hand, it is ascribed to the inception of additional velocity-perturbation streaks locally at the step [1,2]. Such streaks, which are three-dimensional stationary structures, are postulated to be independent of (but triggered and conditioned in wavelength and phase by) the preexisting CFI interacting with the step flow [1,2].

Capitalizing on the periodic nature of perturbations in the leading-edge-parallel direction, Casacuberta *et al.* [1,2] decompose the perturbation field into a set of fundamental (i.e., primary wavelength) and high-order harmonic (i.e., smaller wavelength) spanwise (Fourier) modes. This class of modal decomposition reveals that near-wall streaks actually manifest in each spanwise mode, that is, multiple-wavelength streaks coexist just downstream of the step. Based on this observation, Casacuberta *et al.* [2] hypothesize that each incoming (spanwise) crossflow mode induces an associated near-wall streaky structure when interacting with the step flow, which adopts the spanwise wavelength of the corresponding incoming mode [1]. The *amplitude* of the new

near-wall streaks close to the surface of the step and the incoming CFI that evolves at a larger distance from the wall is thus captured within the shape of the same Fourier mode. Correspondingly, the streaks manifest as an additional peak in the modal perturbation shape, as initially observed by Tufts *et al.* [3]. As such, to segregate between features of the near-wall streaks and the CFI developing above, Casacuberta *et al.* [1] propose to measure *growth* at the upper (i.e., primary) and lower (i.e., secondary) peaks of the modal profile, independently. Using this approach, it was found that the incoming CFI undergoes nonmodal-growth effects in the interaction with the step flow [2]. Whether these newly reported nonmodal effects relate to the local inception of the perturbation streaks remains unexplored.

B. Mechanisms of streak formation in shear flow

Streaky structures are ubiquitous in shear flow [18]. In two-dimensional (i.e., unswept) flow, the mechanisms of streak formation and growth around a forward-facing step have been subject to discussion. This feature has been associated to the lift-up effect [19], as well as to a Görtler type of instability mechanism [20,21]. However, Stüer *et al.* [22] indicate that their experiments do not support the latter in that the instability at the step appears to be of a type stronger than classic Görtler instability. Wilhelm *et al.* [23] and Marino and Luchini [24] argue that the streaks do not originate from an absolute instability [25] of the recirculating flow at the step for, at least, the choice of parameters considered by these authors. Instead, Wilhelm *et al.* [23] ascribe the origin of streaks to a sensitive reaction of the flow to incoming three-dimensional perturbations. This is argued to be a linear perturbation effect, inasmuch as the intensity of streaks changes proportionally to that of incoming perturbations [23].

Such a discussion of mechanisms of modal vs nonmodal perturbation growth is ubiquitous in studies of shear-flow instability. The role of both mechanisms in giving rise to near-wall streaks at the step will be explored in the present work. As such, main preliminary concepts are introduced next. A modal growth mechanism governs the evolution of initially small-amplitude perturbations, which evolve alike the background base flow, experiencing amplification of all velocity components by a common growth rate [26] in the limit of parallel-flow approximation. The reader is referred to Bottaro and Luchini [27] for a discussion on the conditions by which the concept of an asymptotically evolving eigenmode is tenable, in the context of Görtler instability. In contrast, the concept of nonmodal growth stems from the fact that the linear operator governing the evolution of small-amplitude perturbations is nonnormal in certain flow cases; i.e., it has nonorthogonal eigenfunctions [28–30]. The latter implies that the perturbation dynamics cannot be described by a single eigenmode or unique growth rate.

A key physical mechanism giving rise to large nonmodal growth in shear flow is the so-called lift-up effect [31–33]; see Brandt [18] for a review of the topic. The lift-up effect entails the displacement of fluid particles by a three-dimensional cross-stream perturbation which, by retaining their streamwise momentum, increases the kinetic energy of streamwise-perturbations significantly. This phenomenon is commonly exemplified by *small-amplitude* streamwise counterrotating vortices which, superimposed on a shear layer, induce elongated streamwise streaks of high- and low-momentum fluid [34]. The pioneering study of Ellingsen and Palm [31] described the nonmodal growth of streaks in time. Analogous interpretations of the lift-up effect have also been formulated in space [35,36]. Particularly for a three-dimensional boundary layer with *strong* crossflow velocity, it is well established that the base flow supports significant nonmodal growth of localized perturbations [37] for a relatively short finite spatial extent. Such *transient* growth can trigger the formation of modal crossflow vortices, for instance, when localized roughness is present [38], which develop further following a classic growth mechanism of the Orr-Sommerfeld type. In other words, modal and nonmodal growth mechanisms are complementary to each other in that they excite similar structures in a perturbation sense [39,40], namely, alternating streaks of high- and low-momentum fluid [37]. The reader is referred to Casacuberta *et al.* [41, Fig. 6] for a visual representation of both *asymptotic* and *short-term* streamwise streaks in swept-wing flow.

Marxen *et al.* [26] employ a set of diagnostic metrics to segregate between mechanisms of modal and nonmodal growth in a two-dimensional separating laminar boundary layer over a flat plate. This flow environment is similar to the present swept forward-facing step. In both scenarios, the boundary layer is subject to a favorable-to-adverse pressure gradient and a recirculating-flow region develops [2–4,26]. Marxen *et al.* [26] describe the development of three-dimensional streak-like perturbations. They conclude that nonmodal growth ascribed to the lift-up effect governs the perturbation response initially. More downstream, in the adverse-pressure-gradient region, a modal instability of Görtler type sets in as the dominant perturbation mechanism. To segregate between essentially modal- and nonmodal-growth regimes, Marxen *et al.* [26] decompose the perturbation vector into components tangential and normal to the *local* base-flow orientation (i.e., the local base-flow vector) instead of tangential and normal to the wall. While nonmodal growth by the lift-up effect favors the amplification of the flow-aligned perturbation component, in the case of a modal instability, all perturbation components ought to exhibit a similar growth rate [26].

A similar decomposition of the perturbation vector is employed by Lanzerstorfer and Kuhlmann [19] to scrutinize the mechanisms of energy transfer between stationary perturbations and base flow in unswept forward-facing-step flow. More specifically, following the methodology of Albensoeder *et al.* [42], Lanzerstorfer and Kuhlmann [19] decompose the production term of the Reynolds-Orr equation [30] by expressing the perturbation vector into components tangential and normal to the local base-flow orientation. A main term stemming from this decomposition characterizes the lift-up effect [19,43–45], that is, the kinetic-energy transfer rate between base flow and streamwise (i.e., flow aligned) perturbations by the action of the cross-stream (i.e., flow orthogonal) perturbations. The term holds a dominant contribution around the step, thus Lanzerstorfer and Kuhlmann [19] argue that the lift-up effect contributes mainly to the amplification of stationary streaks in unswept step flow. Similar analysis and interpretation have been used in studies of cavity flow [42,45]. Recently, Casacuberta *et al.* [41] have expanded upon the model of perturbation production of Lanzerstorfer and Kuhlmann [19] to characterize the mechanisms of local CFI growth (i.e., a classic lift-up effect) and decay (i.e., a so-called *reverse* lift-up effect) in the interaction with three-dimensional step flow.

As evident by the previous discussion, the salient mechanisms of swept-wing boundary-layer instability due to a surface step are currently under debate [3–5,16]. Among the complex features within the developing flow, velocity streaks appear to hold a critical role towards premature transition [6]. Nevertheless, there is currently no consensus among past works regarding the origin and the nature of these streaks. Elucidating these effects forms the main objective of the present work. Direct numerical simulations (DNS) are employed to explore the mechanisms of instability growth producing stationary spanwise-periodic velocity-perturbation streaks in swept laminar incompressible forward-facing-step flow. The analysis is mainly focused on, but not restricted to, boundary-layer flow with a critical stationary crossflow perturbation. Here critical refers to the integrally most amplified perturbation towards the end of the domain. To further gain a handle on the role of linearity in these processes, results from DNS are compared with linear stability analyses performed through the efficient harmonic Navier-Stokes (HNS) method [46–48]. As will be shown, a linear nonmodal-growth mechanism associated to the lift-up effect is found to be primarily responsible for the rapid inception of streaks at the upper step corner. Additional numerical investigations are performed for varying the effective sweep angle in the flow and incoming perturbation wavelength. Structurally similar perturbation streaks are found to develop in all cases. This points towards the universal presence of streaks in forward-facing-step flow, whose wavelength and initial amplitude is set by pertinent perturbations in the incoming boundary layer.

This article is structured as follows: Sec. II introduces the flow problems, notation, and numerical setups and compares the results between DNS and HNS. Section III describes qualitatively and quantitatively the perturbation evolution at the step. Section IV scrutinizes the instability mechanisms governing the inception and initial evolution of the perturbation streaks. Section V analyzes

effects of spanwise velocity and spanwise wave number. Section VI presents the conclusions of this work.

II. METHODOLOGY

A. Definition of flow problems and notation

In this work, velocity-perturbation streaks in swept forward-facing-step flow are explored by means of direct numerical simulations (DNS). A forward-facing step of fixed height, h, is considered, which is immersed in a three-dimensional swept-wing boundary layer modulated by a preimposed stationary crossflow perturbation. The swept-wing flow is modeled numerically as flat-plate flow (i.e., neglecting wall-curvature effects) with a prescribed static pressure distribution obtained from experiments on a 45° swept wing [5]. While convex wall curvature is known to have a stabilizing effect on the crossflow perturbation [49], the scope of this work is specific to the local mechanisms of streaks at the step, and, as such, it is neglected.

Simulations are performed in a computational domain that mimics the conventions that accompany the reference wing model [5]. Specifically, normal vectors of inflow and outflow planes are arranged to point in the leading-edge-normal (or chordwise) direction, x. The normal vectors of the transverse boundaries point in the leading-edge-parallel (or, spanwise) direction, z, and the wall-normal direction, y, completes the Cartesian coordinate system, $\boldsymbol{x} = [x\ y\ z]^{\mathrm{T}}$. The dimensional width of the computational domain in z is 7.5 mm and equals the spanwise wavelength of the crossflow eigenmode preimposed at the inlet, denoted by λ_z. The inlet is placed at an equivalent 5% of the chord of the reference wing model. To account for effects of sweep angle in the DNS, a globally constant free-stream-velocity component in the direction z (denoted by w_∞) is prescribed at the inflow boundary, together with a free-stream-velocity component in the direction x (denoted by u_∞). The choices of free-stream-flow orientation (w_∞/u_∞) considered in this article are defined in Sec. II B. The parameters $u_\infty = 15.10$ m/s and $\delta_0 = 7.71 \times 10^{-4}$ m, i.e., the 99% inflow boundary-layer thickness associated to u_∞, are used for nondimensionalization purposes. The relevant Reynolds numbers are $\mathrm{Re}_h = u_\infty h/\nu = 769.51$ and $\mathrm{Re}_{hh} = u_h h/\nu = 832.08$, where ν indicates kinematic viscosity and u_h is the chordwise velocity of the clean (i.e., no-step present) boundary layer at the height of the step.

The location of the step in the chordwise direction, $x = 177.62\delta_0$, and the height of the step, $h = 0.97\delta_0$, are fixed in this work. The former corresponds to an equivalent 20% of the chord of the reference wing model, and the latter represents approximately 50% of the clean (i.e., no-step present) boundary-layer thickness at $x = 177.62\delta_0$. The coordinate $x_{\mathrm{st}} = x - 177.62\delta_0$ is hereafter introduced to expresses the relative chordwise distance to the step (i.e., $x_{\mathrm{st}} = 0$ denotes the step location). The upper step corner, i.e., $(x_{\mathrm{st}}, y) = (0, h)$, will also be referred to as *the step apex*. The strength of perturbation streaks in forward-facing-step flow increases with the height of the step [2]. The present choice of step height produces sufficiently amplified streaks, which is beneficial for characterization purposes.

The flow field $\boldsymbol{q} = [u\ v\ w\ p]^{\mathrm{T}} = [\boldsymbol{v}\ p]^{\mathrm{T}}$ is decomposed into the steady unperturbed laminar base flow, $\boldsymbol{q}_B = [u_B\ v_B\ w_B\ p_B]^{\mathrm{T}} = [\boldsymbol{v}_{\mathrm{B}}\ p_{\mathrm{B}}]^{\mathrm{T}}$, and a stationary perturbation field, $\boldsymbol{q}' = [u'\ v'\ w'\ p']^{\mathrm{T}} = [\boldsymbol{v}'\ p']^{\mathrm{T}}$, such that

$$\boldsymbol{q} = \boldsymbol{q}_B + \boldsymbol{q}'. \tag{1}$$

In this work, $\boldsymbol{q}$ will be referred to as the *steady developed flow*. Numerical investigations of swept-wing boundary-layer flow are performed typically under the assumption of *infinite wings*; that is, the base flow is assumed to be spanwise invariant ($\partial \boldsymbol{q}_B/\partial z = 0$). The assumption of spanwise invariance lends itself to the definition of two derivative assumptions, namely, flow periodicity and null perturbation growth in z. Here u, v, and w, denote velocity components in the x, y, and z directions, respectively, and p is the static pressure.

TABLE I. Definition of flow cases. Forcing amplitude refers to the amplitude of the inflow mode in case Baseline and to the amplitude of blowing suction at the wall in cases Test.

Case	w_∞/u_∞	$\lvert\phi_s(0)\rvert$	Forcing method	Forcing amplitude
Baseline	-1.241	51.136°	Inflow mode ($x = 0$)	$3.5 \times 10^{-3} u_\infty$
Test A	-1.241	51.136°	Blowing suction ($x = 140\delta_0$)	$1 \times 10^{-5} u_\infty$
Test B	-0.993	44.791°	Blowing suction ($x = 140\delta_0$)	$1 \times 10^{-5} u_\infty$
Test C	-0.745	36.670°	Blowing suction ($x = 140\delta_0$)	$1 \times 10^{-5} u_\infty$
Test D	-0.496	26.398°	Blowing suction ($x = 140\delta_0$)	$1 \times 10^{-5} u_\infty$
Test E	-0.248	13.938°	Blowing suction ($x = 140\delta_0$)	$1 \times 10^{-5} u_\infty$
Test F	0	0°	Blowing suction ($x = 140\delta_0$)	$1 \times 10^{-5} u_\infty$

Capitalizing on the periodic nature of $\boldsymbol{v}'$ in the spanwise direction, it is instructive to decompose it as

$$\boldsymbol{v}'(x, y, z) = \sum_{j=-N}^{N} \underbrace{\tilde{\boldsymbol{v}}_{(0,j)}(x, y)\, \mathrm{e}^{\mathrm{i}j\beta_0 z}}_{\boldsymbol{v}'_{(0,j)}}, \tag{2}$$

i.e., into a set of fundamental, $\beta = \beta_0$, and high-order harmonic, $\beta = j\beta_0$, $j \geqslant 2$, spanwise perturbation modes. The term *fundamental* refers to the wavelength of the primary crossflow eigenmode, $\lambda_z = 2\pi/\beta_0$; see Casacuberta *et al.* [2] for details on the choice of preimposed perturbation wavelength. In Eq. (2), N indicates (one-half of) the number of modes, $\tilde{\boldsymbol{v}}_{(0,j)} = [\tilde{u}_{(0,j)}\ \tilde{v}_{(0,j)}\ \tilde{w}_{(0,j)}]^{\mathrm{T}} \in \mathbb{C}^3$ expresses the Fourier (or amplitude) coefficient, and $\mathrm{i}^2 = -1$. It is noted that $\boldsymbol{v}'_{(0,-j)} = \boldsymbol{v}'^{\dagger}_{(0,j)}$, where the symbol "†" denotes the complex conjugate (c.c.) operation. The mode $\boldsymbol{v}'_{(0,0)}$ comprises the nonoscillatory perturbation content, and, as such, it is referred typically to as the mean-flow distortion. The moduli of the components of $\tilde{\boldsymbol{v}}_{(0,j)}$, the so-called amplitude functions, are expressed as $|\tilde{u}|_{(0,j)}$, $|\tilde{v}|_{(0,j)}$, and $|\tilde{w}|_{(0,j)}$. Finally, the spatial growth rate in x of a perturbation feature of spanwise wave number $j\beta_0$ is evaluated as

$$\alpha^q_{i,(0,j)} = -\frac{1}{|\tilde{q}|^{y=y^l}_{(0,j)}} \frac{\mathrm{d}|\tilde{q}|^{y=y^l}_{(0,j)}}{\mathrm{d}x}. \tag{3}$$

In Eq. (3), q represents a chosen quantity, such as perturbation velocity, and y^l refers to the wall-normal location at which *amplitude* is measured in its corresponding amplitude function; Sec. III B elaborates on the choices of y^l to unequivocally establish a measure of *growth*. Considering that multiple perturbation structures coexist at the step, integral metrics in y potentially masking individual mechanisms are not utilized in this work.

B. Free-stream and incoming perturbation conditions

The ratio of spanwise to chordwise free-stream velocity imposed at inflow, w_∞/u_∞, in the DNS establishes the orientation of inviscid streamlines, in essence defining the effective sweep angle. The main case discussed in this work (i.e., case Baseline in Table I) considers $w_\infty/u_\infty = -1.241$, which is guided by experiments of Rius-Vidales and Kotsonis [5]. To assess spanwise-velocity effects in the mechanisms of perturbation interaction at the step, additional simulations are carried out, in which the value of w_∞ is increased gradually from $-1.241u_\infty$ to 0 in fixed steps of Δw_∞. These secondary cases are referred to as Test A–F in Table I. By virtue of decoupling of the x-momentum conservation equation from the z-momentum conservation equation in a spanwise-invariant flow, the present approach yields identical representation of chordwise-velocity evolution among cases Test A–F (Table I). Specifically, by fixing the chordwise velocity, the chordwise Reynolds number

associated to the step location is also fixed. Hence, effects on the streaks of the crossflow (i.e., the secondary flow orthogonal to the direction of inviscid streamlines) in the immediate vicinity of the step may be isolated. However, it is noted that the *global* Reynolds number based on the total free-stream velocity, $\sqrt{u_\infty^2 + w_\infty^2}$, changes throughout case Test A–F in Table I. In addition, Table I reports the angle at inflow ($x = 0$) that the inviscid streamlines form locally with the x direction, which is denoted by ϕ_s, and relevant features of the perturbation forcing.

Cases Baseline and Test (Table I) consider different methods to trigger stationary instability growth preexisting upstream of the step. This stems from the fact that changing w_∞ inherently alters the nature of incoming boundary-layer perturbation response (but not, in essence, the inception of streaks at the step). For the Baseline case, the stationary CFI is triggered by disturbing the DNS inflow with a stationary crossflow eigenmode precomputed as a solution to the local Orr-Sommerfeld stability problem. The mode is assigned a maximum finite amplitude, $3.5 \times 10^{-3} u_\infty$, which reproduces identically the perturbation environment of Casacuberta et *al.* [2]. This approach is referred to as "inflow mode" in Table I. The present choice of initial amplitude yields linear evolution of the fundamental CFI until approximately the virtual x position of the step in reference conditions.

The cases designed as Test in Table I are governed by varying sweep angle to the limit of unswept ($w_\infty = 0$) conditions. In this limiting case of two-dimensional flow, the concept of an asymptotically evolving crossflow eigenmode is not tenable. However, to sustain comparison between cases Test in terms of streak characterization at the step, a stationary perturbation ought to preexist in all cases. Capitalizing on its *structural similarity* with the stationary CFI, a stationary Klebannof mode is thus excited upstream of the step in cases designated as Test with *small* sweep angle (Table I). So-called Klebanoff modes [50,51] are boundary-layer perturbations typically found in scenarios of natural bypass transition [52–55]. Despite the original name, Klebanoff modes do not appear as solutions to a local eigenvalue analysis [56] since they do not actually represent an eigensolution or *mode* of a response equation [54,57]. At a perturbation level, both the stationary CFI and stationary Klebanoff modes manifest topologically as spanwise-distributed regions of streamwise-velocity deficit and excess accompanied by a weak cross-stream perturbation component [9,56]. This topological similarity is key to sustaining comparison across all cases discussed in this work since both incoming perturbation types trigger the same mechanisms of streak inception at the step (Sec. V A).

By use of the parabolized stability equations (PSE) method, Herbert [56] shows that stationary Klebanoff modes may be excited through a local spanwise modulation of the wall-shear stress. In this work, a stationary Klebanoff mode is excited via blowing suction at the wall. This is enabled in the present DNS by altering the no-penetration condition at $y = 0$ and locally modulating the wall-normal velocity as

$$v(x, 0, z) = A_0 f_f(x) \cos(\beta_0 z) \tag{4}$$

with

$$f_f(x) = \left(\frac{4(x - x_{\text{start}})(x_{\text{end}} - x)}{(x_{\text{end}} - x_{\text{start}})^2} \right)^3. \tag{5}$$

In Eq. (4), A_0 is the amplitude of the spanwise modulation and f_f is a function that smoothly adjusts the steady wall forcing in the x direction between its starting, $x_{\text{start}} = 136\delta_0$, and ending, $x_{\text{end}} = 144\delta_0$, positions, both placed upstream of the step. It is noted that f_f has vanishing first and second derivatives at $x = x_{\text{start}}$ and x_{end} and represents a symmetrical distribution. For the cases designated as Test (Table I), the use of steady blowing suction as the forcing method leverages the receptivity of the flow to a stationary CFI for large w_∞/u_∞ and to a Klebanoff mode for small w_∞/u_∞. A common spanwise wavelength, $\lambda_z = 7.5$ mm, and amplitude of blowing suction, $A_0 = 1 \times 10^{-5} u_\infty$ [Eq. (4)], is applied in all cases Test (Table I). The choice of a relatively low-amplitude value prevents the appearance of potential nonlinear perturbation effects within the step interaction region. This is further reconciled in Sec. II D, where it will be shown that the streaks are a feature of the linear perturbation equations.

C. Setup of the DNS

The DNS in the present work are carried out with the conservative finite-volume solver INCA [58]. This solver has been employed in previous numerical investigations of low-speed boundary-layer instability involving isolated [59] and distributed [2] surface features. In particular, the present DNS setup is largely similar to that employed by Casacuberta *et al.* [2], to which the reader is referred to for main details on the numerical discretization and solution methods, grid topology, and boundary conditions applied. Major differences with the setup of this work are highlighted next.

The dimensions of the computational domain are $0 \leqslant x/\delta_0 \leqslant 245$, $0 \leqslant y/\delta_0 \leqslant 26$, and $-4.86 \leqslant z/\delta_0 \leqslant 4.86$. Two main families of simulations are carried out in a sequential manner, namely, steady-state computations of the unperturbed base flow, $\boldsymbol{q}_\mathrm{B}$, and steady-state computations of the developed flow, $\boldsymbol{q}_\mathrm{B} + \boldsymbol{q}'$ [Eq. (1)]. In the latter case, a corresponding perturbation forcing method (Table I) is switched on. The incompressible Navier-Stokes equations are marched in time with an explicit third-order Runge-Kutta method. A convergence threshold of value $\epsilon = 10^{-9}$ for the L_2 norm of temporal derivatives in the domain is chosen, while the pressure Poisson equation is solved using the BiCGstab method and converged up to a threshold of $\epsilon_\mathrm{DIV} = 10^{-10}$. The time-converged base flow $\boldsymbol{q}_\mathrm{B}$ forms the initial condition for subsequent simulations of the steady developed flow.

Capitalizing on the invariance of $\boldsymbol{q}_\mathrm{B}$ in z, two grid points ($N_z = 2$) are considered along the span in the base-flow computations. Contrarily, $N_z = 72$ for computations of the developed flow, which ensures sufficient grid resolution to accurately resolve the evolution of steady perturbations [2]. Additionally, the computational grid contains $N_x = 5000$ points in the chordwise direction; in the wall-normal direction, $N_y = 1152$ grid points are placed upstream of the step and $N_y = 1008$ are placed downstream of it. A high level of grid refinement in the near-wall region around the step is ensured to accurately resolve the localized evolution of the perturbation streaks. The good agreement in terms of perturbation evolution between the results from DNS and independent stability analyses (see Sec. II D) provides confidence in the choice of grid topology and density.

D. Setup of HNS

In this work, effects of spanwise wavelength on the mechanisms of the streaks at the step are assessed through stability analysis. Parametric studies of incoming instability specifications, as well as other critical parameters such as the Reynolds number, require efficient simulation tools. The parabolized stability equations (PSE) (see Bertolotti *et al.* [60] and Herbert [56]) or the Orr-Sommerfeld equation [7,61,62] are classic methods for efficient stability calculations. However, these methods suffer from limitations in highly nonparallel flow such as the present step flow; see also the discussion by Casacuberta *et al.* [2] on nonmodal growth effects at the step. In particular, Casacuberta *et al.* [2] highlight the inability of modal stability methods to capture the formation of the streaks at the step.

To overcome these aforementioned limitations, the harmonic Navier-Stokes method (HNS) is employed in this work to assess the stability of the step flow. The HNS is an efficient approach to instability modeling considering the full form of Navier-Stokes equations with one or more directions of harmonic perturbation evolution, i.e., the z direction in the present flow problem. Considering the scope of this work, the HNS allows for the modeling of both nonmodal and nonparallel effects at the step without preimposed assumptions on the class of growth mechanisms that develop. Moreover, the computational cost of the HNS is significantly reduced compared to DNS, which is key to produce a large data set of perturbation fields. In one of the first works featuring HNS computations, Choudhari and Streett [63] studied the receptivity process of crossflow instabilities and the effect of curvature. Guo *et al.* [64] later introduced a streamwise wave number in the perturbation ansatz to reduce the grid requirements. The HNS has been shown to closely match PSE predictions for several flow configurations without rapid variations of surface geometry, e.g., Blasius, swept-wing, and Hiemenz flows [64], as well as to outperform PSE when rapid variations are present [65,66].

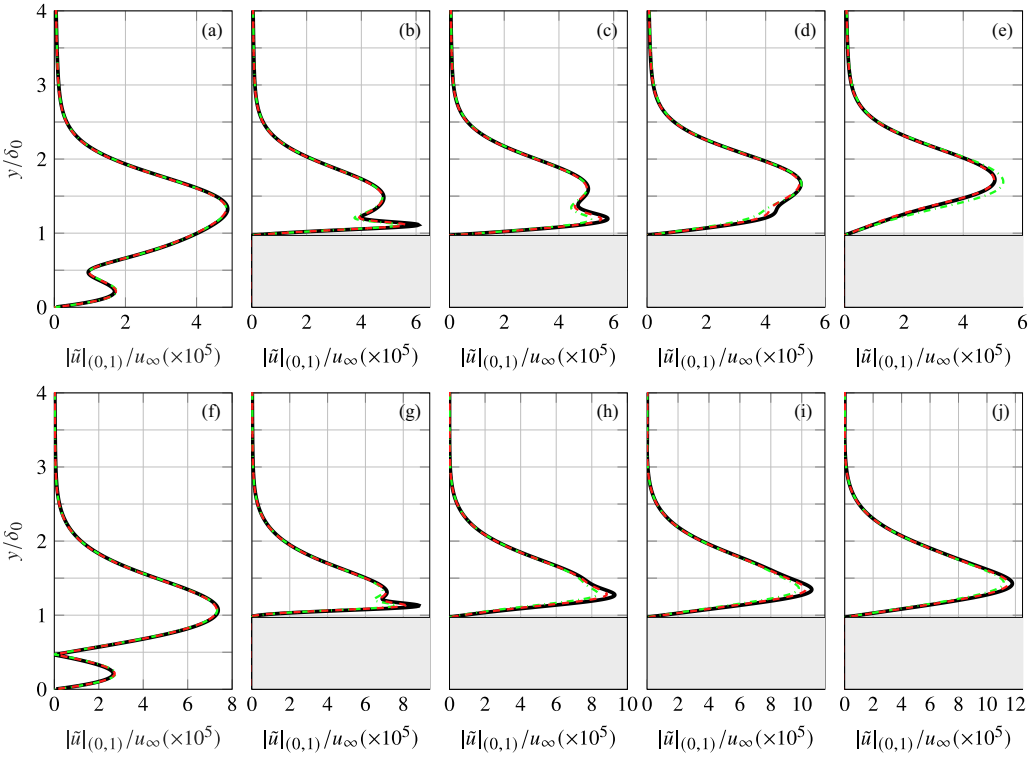

FIG. 1. Profiles along y of the amplitude function $|\tilde{u}|_{(0,1)}$ at the step from DNS (solid black), AHLNS (dash-dotted green), and DeHNSSo (dashed red) at $x_{st}/\delta_0 = -0.5$ [(a), (f)], 0.5 [(b), (g)], 2.5 [(c), (h)], 5 [(d), (i)], 10 [(e), (j)]. Top row illustrates case $\max(|w_\infty/u_\infty|)$ and bottom row illustrates case $w_\infty/u_\infty = 0$.

Two different HNS frameworks have been utilized in this work to strengthen the comparison with DNS, namely, the Delft harmonic Navier-Stokes Solver, DeHNSSo [48], and the adaptive harmonic linearized Navier-Stokes (AHLNS) [46,47]. Henceforth, they are jointly referred to as (AL)HNS for convenience. Both frameworks solve the linear HNS equations, but feature implementation differences; see the discussion in Franco and Hein [67]. The DeHNSSo is a pseudospectral method involving spectral differentiation in the wall-normal direction, whereas AHLNS is fully finite-difference based. Furthermore, DeHNSSo employs an embedded boundary method to model the step, while AHLNS considers a multiblock grid and follows the so-called adaptive approach introduced by Guo *et al.* [64]. It is noted that the incorporation of a chordwise wave number in the adaptive approach of AHLNS does not constrain the perturbation growth in a modal sense, but is used towards a more effective numerical resolution. The results from DNS and (AL)HNS are compared in this section for validation purposes. The goal of this comparison is twofold; first, to demonstrate the accuracy of (AL)HNS methods for stability calculations in highly nonparallel (step) flows and, second, to provide confidence in the numerical setup and choices of grid resolution.

Figure 1 portrays profiles of the fundamental chordwise-velocity perturbation amplitude function, $|\tilde{u}|_{(0,1)}$ (Sec. II A), at different x locations obtained from AHLNS (dash-dotted green), DeHNSSo (dashed red), and DNS (solid black). It is noted that Figs. 1(a)–1(e) represent $\max(|w_\infty/u_\infty|)$ conditions (i.e., Test A in Table I) and Figs. 1(f)–1(j) represent $w_\infty/u_\infty = 0$ conditions (i.e., Test F in Table I). The present calculations consider a spanwise perturbation wavelength of $\lambda_z = 7.5$ mm. The growth and further decay in x of near-wall perturbation streaks close downstream of the step is well captured by (AL)HNS. Minor differences between DeHNSSo and AHLNS are noted in the amplitude of the streaks just after their point of inception. It is

emphasized that a match between methods in Fig. 1 is obtained despite the inherent assumption of linearity in (AL)HNS; that is, the (AL)HNS methods seek numerical solutions to the linearized form of the perturbation equations. The present match of DNS with linear methods is likely contingent upon the use of a *small* amplitude of the incoming CFI (Table I). For a larger amplitude, the inherently linear perturbation streaks may undergo nonlinear effects farther downstream of the step. However, the latter is out of the scope of this work.

III. OVERVIEW OF PERTURBATION EVOLUTION AT THE STEP

A. Perturbation organization

The analysis of results is commenced by presenting an overview of the perturbation evolution at the step in the Baseline case (see Table I). Concerning the overarching subject of this work, stationary spanwise-harmonic velocity-perturbation streaks of wave numbers $\beta = j\beta_0$, $j = 2, \ldots, N$, form and coexist in the downstream vicinity of the step. As such, a streaky structure manifests in each spanwise perturbation mode [Eq. (2)]. Topologically, the streaks appear as alternating regions of velocity excess and deficit distributed along the step-edge direction, z. They develop spatially very close to the wall. A main goal of this work is to explore the origin and evolution of the streaks at the step. To isolate pertinent effects, a distinction is made in the following analysis between the fundamental, $j = 1$, and high-order harmonic, $j \geqslant 2$, perturbation streaks. For simplicity, the main body of the discussion focuses first on fundamental streaks. Later, in Sec. IV D, mechanisms of the perturbation streaks of higher order will be discussed.

Figure 2 portrays the three-dimensional organization of the fundamental velocity-perturbation fields, $u'_{(0,1)}$, $w'_{(0,1)}$, and $v'_{(0,1)}$. For all velocity components, the main structure of the incoming perturbation, i.e., the stationary CFI, lifts off the wall gradually as it approaches the step [2–5]. Casacuberta *et al.* [2] provide a discussion on the three-dimensional organization of the perturbation field at the step, in relation to that of base-flow streamlines. Just after passing the upper step corner, the near-wall portion of the stationary perturbation field is amplified significantly, when compared to conditions far upstream of the step [3,4]; see also Fig. 2. As elaborated upon in Sec. IV A, this effect manifests more prominently in the chordwise-velocity component, $u'_{(0,1)}$, as strongly amplified oval-shaped $u'_{(0,1)}$ streaks located underneath the incoming CFI are evident (Fig. 2). For the choice of step height and strength of the incoming CFI considered in this work, the amplitude of near-wall streaks forming at the step decays downstream in x, with the streaks ultimately vanishing [Fig. 2(a)]. It is noted that near-wall velocity-perturbation streaks form as well in the upstream vicinity of the step; see Fig. 2. However, they appear to originate independently from the streaks downstream of the step, as they mainly reside in the locally separating flow upstream of the step. The focus of this work is specifically placed on the streaky structures forming downstream of the step, where premature laminar-turbulent transition has been reported [4,5,16].

B. Quantification of perturbation growth

In CFI-dominated problems, the amplitude function of a single velocity-perturbation component (e.g., $|\tilde{u}|_{(0,1)}$) is employed typically to quantify perturbation growth and decay; see Sec. II A for definitions of modal quantities. However, as shown in the section above, the perturbation fields $u'_{(0,1)}$, $v'_{(0,1)}$, and $w'_{(0,1)}$ exhibit essentially different growth rates in x in the vicinity of the step. As such, to quantify perturbation evolution in a *global* exploratory sense, perturbation growth is evaluated here based on the norm of the *total* perturbation velocity vector.

This is illustrated as follows: given a stationary mode $\beta = j\beta_0$, $j = 1, \ldots, N$, the norm of the perturbation velocity vector at every point in space reads

$$||\boldsymbol{v}'_{(0,j)}|| \equiv |\tilde{\psi}|_{(0,j)} = \sqrt{|\tilde{u}|^2_{(0,j)} + |\tilde{v}|^2_{(0,j)} + |\tilde{w}|^2_{(0,j)}}. \tag{6}$$

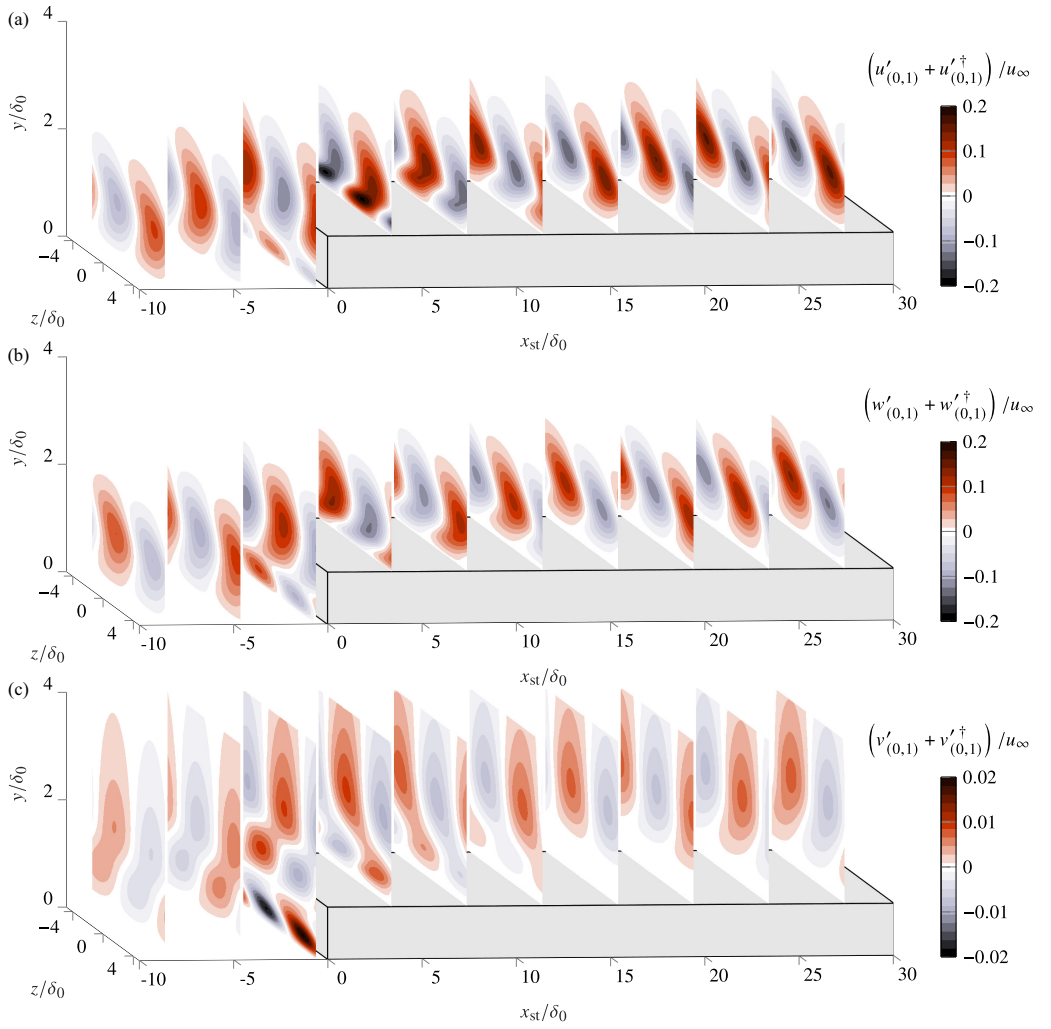

FIG. 2. Organization of the chordwise (a), spanwise (b), and wall-normal (c) fundamental velocity-perturbation fields ($\beta = \beta_0$). Note the different scale in plot (c).

Figure 3(a) portrays the evolution of $|\tilde{\psi}|_{(0,1)}$. In turn, $|\tilde{\psi}|_{(0,j)}$ relates to the kinetic energy of the mode $j\beta_0$, at a given x location, as

$$E_{j\beta_0} = \frac{1}{2}\int_0^\infty |\tilde{\psi}|^2_{(0,j)}\,\mathrm{d}y. \tag{7}$$

As previously observed by Tufts *et al.* [3], the perturbation shape (i.e., the profile along y of typically $|\tilde{u}|_{(0,1)}$) develops a secondary peak after passing the step in x, which is a feature also observed in the present simulations. A secondary near-wall peak forms as well in the profiles of the *total* amplitude function, $|\tilde{\psi}|_{(0,1)}$ [Eq. (6)]. Due to this, the use of amplitude metrics derived from an integral energy quantity in y as in Eq. (7) blends perturbation effects at the step. Monitoring growth at selected wall-normal locations is hence deemed necessary: amplitude measured at the wall-normal location of the peak closer to the wall quantifies the amplification of streaks in x, while amplitude measured at the wall-normal location of the upper (preexisting) peak quantifies the evolution of the original CFI [1].

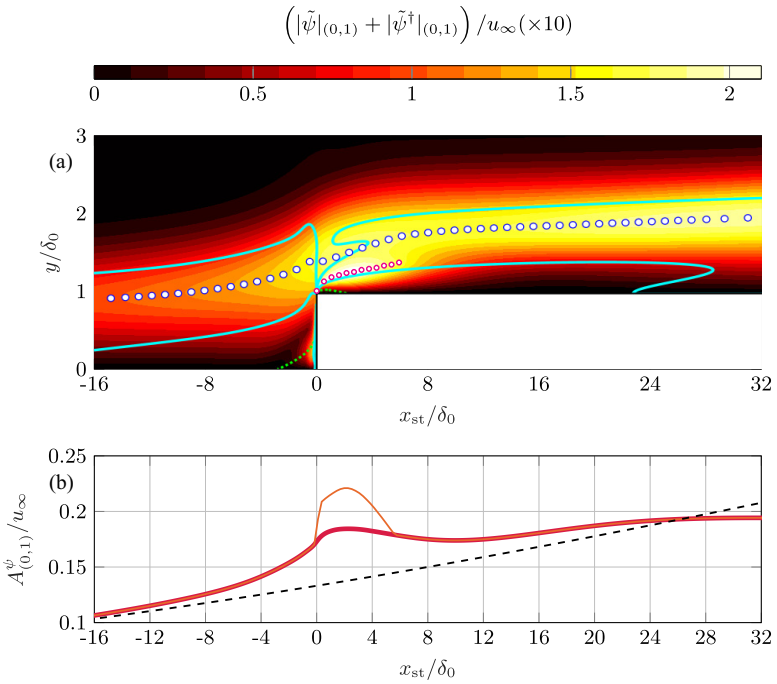

FIG. 3. Flow features at the step (a): fundamental amplitude function $|\tilde{\psi}|_{(0,1)}$ (color contour), wall-normal position of primary (i.e., associated to $|\tilde{\psi}|^{\rm top}_{(0,1)}$, big blue circles) and secondary (i.e., associated to $|\tilde{\psi}|^{\rm str}_{(0,1)}$, small magenta circles) perturbation peaks, loci of base-flow crossflow inflection points (solid cyan), and base-flow reversal $u_{\rm B} = 0$ (dotted green) reproduced from Casacuberta *et al.* [2]. Chordwise evolution of perturbation *amplitude* (b): $A^{\psi}_{(0,1)} = |\tilde{\psi}|^{\rm max}_{(0,1)}$ in the step (thin solid orange) and reference no-step (thin dashed black) cases, $A^{\psi}_{(0,1)} = |\tilde{\psi}|^{\rm top}_{(0,1)}$ in the step case (thick solid red).

The main goal of this work is to elucidate the origin of near-wall streaks at the step. As such, stability features are quantified mainly at the wall-normal location of the lower perturbation peak that forms close to the wall just downstream of the step in x. Amplitude measured at the upper peak is denoted by $|\tilde{q}|^{\rm top}_{(0,1)}$, amplitude measured at the lower peak arising downstream of the step is denoted by $|\tilde{q}|^{\rm str}_{(0,1)}$, and amplitude locally measured at the largest peak for every x is denoted by $|\tilde{q}|^{\rm max}_{(0,1)}$; here q indicates a selected quantity such as u or ψ. The wall-normal location of $|\tilde{\psi}|^{\rm str}_{(0,1)}$ is henceforth denoted as $\tilde{y}^{\psi,{\rm str}}_{(0,1)}$. A graphical representation of these metrics is shown in Fig. 3(b). The thin solid orange line illustrates an amplitude characterization based on the global maximum of $|\tilde{\psi}|_{(0,1)}$ in y. This amplitude metric inherently characterizes growth of the near-wall streaks just downstream of the step, but growth of the crossflow perturbation farther from it [1]. The thick solid red line depicts the evolution in x of the amplitude of the original CFI, exclusively.

C. Perturbation decomposition relative to the base-flow orientation

To further explore mechanisms of shear-flow instability, a decomposition of the perturbation vector relative to the local orientation of base-flow streamlines, rather than relative to the wall, is used [2,19,26,42,44,45]. This approach is especially appealing for this work due to the large deformation of base-flow streamlines around the step [4,5]. The essence of the aforementioned perturbation decomposition in the present spanwise-invariant three-dimensional base flow is illustrated

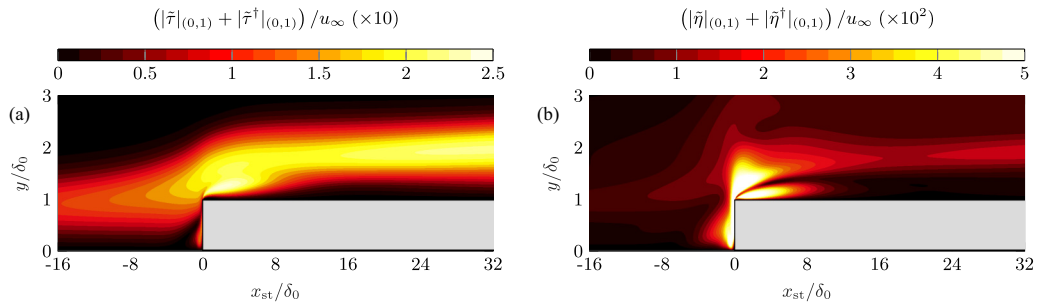

FIG. 4. Amplitude function of fundamental (a) streamwise, $|\tilde{\tau}|_{(0,1)}$, and (b) cross-stream, $|\tilde{\eta}|_{(0,1)}$, velocity perturbations.

as follows: under a classic wall-based decomposition, the perturbation vector reads

$$\boldsymbol{v}'_{(0,1)}(x,y,z) = u'_{(0,1)}(x,y,z)\hat{\boldsymbol{\imath}} + v'_{(0,1)}(x,y,z)\hat{\boldsymbol{\jmath}} + w'_{(0,1)}(x,y,z)\hat{\boldsymbol{k}} \tag{8}$$

with $\hat{\boldsymbol{\imath}} = [1\ 0\ 0]^{\mathrm{T}}$, $\hat{\boldsymbol{\jmath}} = [0\ 1\ 0]^{\mathrm{T}}$, $\hat{\boldsymbol{k}} = [0\ 0\ 1]^{\mathrm{T}}$. Following the approach of Albensoeder *et al.* [42] and Lanzerstorfer and Kuhlmann [19], the perturbation vector is decomposed as

$$\begin{aligned}\boldsymbol{v}'_{(0,1)}(x,y,z) &= \boldsymbol{v}'_{t,(0,1)}(x,y,z) + \boldsymbol{v}'_{n,(0,1)}(x,y,z)\\ &= \left[\upsilon'^{1}_{t,(0,1)}\ \upsilon'^{2}_{t,(0,1)}\ \upsilon'^{3}_{t,(0,1)}\right]^{\mathrm{T}} + \left[\upsilon'^{1}_{n,(0,1)}\ \upsilon'^{2}_{n,(0,1)}\ \upsilon'^{3}_{n,(0,1)}\right]^{\mathrm{T}},\end{aligned} \tag{9}$$

where the superscripts 1, 2, 3, respectively, denote vector components in the x, y, and z directions. In Eq. (9), the vector field $\boldsymbol{v}'_{t,(0,1)} : \mathbb{R}^3 \to \mathbb{C}^3$ characterizes the perturbation acting in the *local* direction of base-flow streamlines, i.e., the streamwise direction $\hat{\boldsymbol{t}} = \boldsymbol{v}_{\mathrm{B}}/||\boldsymbol{v}_{\mathrm{B}}||$ (Sec. II A). For convenience, this may be expressed as

$$\boldsymbol{v}'_{t,(0,1)} = \tau'_{(0,1)}\hat{\boldsymbol{t}}, \tag{10}$$

where $\tau'_{(0,1)}$ is the scalar complex-valued perturbation component in the direction $\hat{\boldsymbol{t}}$. The vector field $\boldsymbol{v}'_{n,(0,1)} : \mathbb{R}^3 \to \mathbb{C}^3$ in Eq. (9) complementarily characterizes the perturbation acting normal to base-flow streamlines, i.e., in the cross-stream direction.

Explicit analytic expressions of $\boldsymbol{v}'_t$, τ', $\boldsymbol{v}'_n$ and details on their mathematical formulation can be found in Casacuberta *et al.* [2,41]. For quantification purposes, amplitude functions can be retrieved for the streamwise, $|\tilde{\tau}|_{(0,1)} \equiv ||\boldsymbol{v}'_{t,(0,1)}||$, and the cross-stream, $|\tilde{\eta}|_{(0,1)} \equiv ||\boldsymbol{v}'_{n,(0,1)}|| = \sqrt{||\boldsymbol{v}'_{(0,1)}||^2 - ||\boldsymbol{v}'_{t,(0,1)}||^2}$, perturbation components [2]. The evolution of $|\tilde{\tau}|_{(0,1)}$ and $|\tilde{\eta}|_{(0,1)}$ around the step is illustrated in Fig. 4.

From a physical standpoint, $\boldsymbol{v}'_t$ and $\boldsymbol{v}'_n$ carry information on two main structural elements of the perturbation field. In the present flow problem, the cross-stream perturbation manifests as rolls, i.e., streamwise-vortical structures. Despite the motion by $\boldsymbol{v}'_n$ having a small amplitude relative to $\boldsymbol{v}'_t$, it is efficient in redistributing streamwise momentum. This produces a *scar* or distortion in the flow that appears as regions of streamwise-velocity excess and deficit ($\boldsymbol{v}'_t$); correspondingly, $\boldsymbol{v}'_t$ encompasses here the main energetic content of the perturbation field. A similar effect is identified for the Görtler instability by Floryan [68]. In swept-wing flow, Saric *et al.* [9] describe that "the weak motion of the [stationary crossflow] wave convects $O(1)$ streamwise momentum producing a strong distortion in the streamwise boundary-layer profile." This manifests in the developed flow, $\boldsymbol{q}_{\mathrm{B}} + \boldsymbol{q}'$ [Eq. (1)], as stationary corotating (crossflow) vortices. For illustration purposes, Fig. 15 in the Appendix portrays y-z planes of the crossflow perturbation far upstream [Fig. 15(a)] and far downstream [Fig. 15(b)] of the step.

IV. ORIGIN AND EVOLUTION OF PERTURBATION STREAKS

This section discusses the mechanisms that drive the growth and initial development of the streaks and whether to classify it as a modal or a nonmodal instability. The focus of Secs. IV A, IV B, and IV C is exclusive to the streaks of fundamental wavelength. In Sec. IV D the analysis is extended to streaks of high-order harmonic wavelength.

A. The role of the lift-up effect

The Reynolds-Orr equation is considered next,

$$\frac{\mathrm{d}E_V}{\mathrm{d}t} = P + D, \tag{11}$$

governing the temporal change of the perturbation kinetic energy, E_V, where $D < 0$ expresses viscous dissipation and P indicates production, i.e., the kinetic energy transfer rate between the unperturbed base flow and the perturbation field as a whole. Equation (11) is formulated considering a localized or spatially periodic perturbation. This leads to the vanishing of several terms, including the nonlinear mechanism or perturbation advection, by virtue of Gauss's theorem [30]. The reader is referred to Casacuberta *et al.* [69] for an extended formulation of the Reynolds-Orr equation considering each spanwise perturbation mode, individually. When evaluated for the fundamental spanwise mode solely, i.e., perturbations with $\beta = \beta_0$ [Eq. (2)], production reads

$$P_{\beta_0} = -\int_V (\boldsymbol{v}'_{(0,1)} + \text{c.c.}) \cdot ((\boldsymbol{v}'_{(0,1)} + \text{c.c.}) \cdot \nabla)\boldsymbol{v}_\text{B} \, \mathrm{d}V = -\frac{2\pi}{\beta_0} \int_S \Lambda_{\beta_0} \, \mathrm{d}x \, \mathrm{d}y. \tag{12}$$

The general equation is obtained by forming the inner product between the pertinent term in the momentum-perturbation equations and the velocity-perturbation vector and integrating over the domain of interest. Due to the $2\pi/\beta_0$ periodicity of the fundamental mode, this volume integral reduces to an integral in the x-y plane. The production term of principal interest reads

$$\begin{aligned}\Lambda_{\beta_0} = {} & (\tilde{u}_{(0,1)}\tilde{u}^\dagger_{(0,1)} + \text{c.c.})\frac{\partial u_\text{B}}{\partial x} + (\tilde{u}_{(0,1)}\tilde{v}^\dagger_{(0,1)} + \text{c.c.})\frac{\partial u_\text{B}}{\partial y} + (\tilde{v}_{(0,1)}\tilde{u}^\dagger_{(0,1)} + \text{c.c.})\frac{\partial v_\text{B}}{\partial x} \\ & + (\tilde{v}_{(0,1)}\tilde{v}^\dagger_{(0,1)} + \text{c.c.})\frac{\partial v_\text{B}}{\partial y} + (\tilde{w}_{(0,1)}\tilde{u}^\dagger_{(0,1)} + \text{c.c.})\frac{\partial w_\text{B}}{\partial x} + (\tilde{w}_{(0,1)}\tilde{v}^\dagger_{(0,1)} + \text{c.c.})\frac{\partial w_\text{B}}{\partial y}.\end{aligned} \tag{13}$$

In Eq. (12), S denotes a x-y cross-sectional surface encompassing the step in x and extending from the wall to the free stream in y. The V is the associated volume extending towards the periodic boundaries in z. From a physical viewpoint, P_{β_0} expresses the kinetic-energy transfer rate in time between the base flow and the fundamental perturbation field, $\boldsymbol{v}'_{(0,1)}$, in the volume V.

Following the approach of Albensoeder *et al.* [42] and Lanzerstorfer and Kuhlmann [19], the production term is decomposed as

$$P_{\beta_0} = I_1^{\beta_0} + I_2^{\beta_0} + I_3^{\beta_0} + I_4^{\beta_0} \tag{14}$$

by introducing the decomposition of Eq. (9) into Eq. (12). Each term $I_m^{\beta_0}$, m = 1-4 in Eq. (14) characterizes a particular mechanism contributing to the exchange of kinetic energy between the base flow and the perturbation field.

The term $I_2^{\beta_0}$ is the lift-up effect [31–33], which is a flow mechanism widely associated to the amplification of streaky structures in shear flow [18]. This mechanism entails the exchange of kinetic energy between the base flow, $\boldsymbol{v}_\text{B}$, and streamwise perturbations, $\boldsymbol{v}'_t$, by the action of cross-stream perturbations, $\boldsymbol{v}'_n$. It reads

$$I_2^{\beta_0} = -\int_V (\boldsymbol{v}'_{t,(0,1)} + \text{c.c.}) \cdot ((\boldsymbol{v}'_{n,(0,1)} + \text{c.c.}) \cdot \nabla)\boldsymbol{v}_\text{B} \, \mathrm{d}V = -\frac{2\pi}{\beta_0} \int_S \Lambda_2^{\beta_0} \, \mathrm{d}x \, \mathrm{d}y, \tag{15}$$

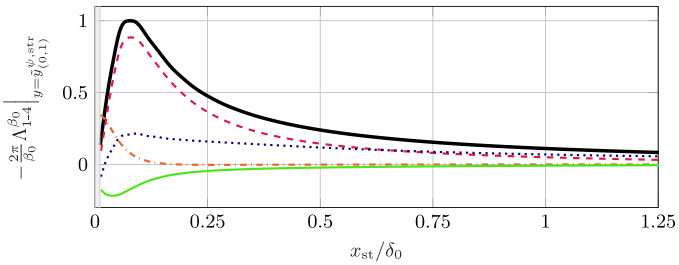

FIG. 5. Chordwise evolution of production terms at the wall-normal location of the core of streaks: $\Lambda_1^{\beta_0}$ (dash-dotted orange), $\Lambda_2^{\beta_0}$ (dashed red), $\Lambda_3^{\beta_0}$ (thin solid green), $\Lambda_4^{\beta_0}$ (dotted blue), and Λ_{β_0} (thick solid black). All curves are normalized relative to maximum Λ_{β_0}.

with

$$\Lambda_2^{\beta_0} = \big(\tilde{v}_t^1\ \tilde{v}_n^{1\dagger} + \mathrm{c.c.}\big)\frac{\partial u_{\mathrm{B}}}{\partial x} + \big(\tilde{v}_t^1\ \tilde{v}_n^{2\dagger} + \mathrm{c.c.}\big)\frac{\partial u_{\mathrm{B}}}{\partial y} + \big(\tilde{v}_t^2\ \tilde{v}_n^{1\dagger} + \mathrm{c.c.}\big)\frac{\partial v_{\mathrm{B}}}{\partial x} + \big(\tilde{v}_t^2\ \tilde{v}_n^{2\dagger} + \mathrm{c.c.}\big)\frac{\partial v_{\mathrm{B}}}{\partial y} + \big(\tilde{v}_t^3\ \tilde{v}_n^{1\dagger} + \mathrm{c.c.}\big)\frac{\partial w_{\mathrm{B}}}{\partial x} + \big(\tilde{v}_t^3\ \tilde{v}_n^{2\dagger} + \mathrm{c.c.}\big)\frac{\partial w_{\mathrm{B}}}{\partial y}, \tag{16}$$

where the subscript (0, 1) has been removed in Eq. (16) for conciseness. The remaining terms

$$I_1^{\beta_0} = -\int_V (\boldsymbol{v}'_{n,(0,1)} + \mathrm{c.c.}) \cdot ((\boldsymbol{v}'_{n,(0,1)} + \mathrm{c.c.}) \cdot \boldsymbol{\nabla})\boldsymbol{v}_{\mathrm{B}}\ \mathrm{d}V \tag{17}$$

and

$$I_4^{\beta_0} = -\int_V (\boldsymbol{v}'_{t,(0,1)} + \mathrm{c.c.}) \cdot ((\boldsymbol{v}'_{t,(0,1)} + \mathrm{c.c.}) \cdot \boldsymbol{\nabla})\boldsymbol{v}_{\mathrm{B}}\ \mathrm{d}V \tag{18}$$

respectively characterize a self-induction mechanism of the cross-stream and streamwise perturbation structures. In particular, the mechanism of I_4 will be referred to in this work as the "push-forward effect" in analogy to the principle of the lift-up effect. Finally,

$$I_3^{\beta_0} = -\int_V (\boldsymbol{v}'_{n,(0,1)} + \mathrm{c.c.}) \cdot ((\boldsymbol{v}'_{t,(0,1)} + \mathrm{c.c.}) \cdot \boldsymbol{\nabla})\boldsymbol{v}_{\mathrm{B}}\ \mathrm{d}V \tag{19}$$

has been associated to a mechanism of perturbation streaks evolving into perturbation rolls [70]. A treatment analogous to Eqs. (15) and (16) may be performed for $I_1^{\beta_0} = (-2\pi/\beta_0)\int_S \Lambda_1^{\beta_0}\ \mathrm{d}x\,\mathrm{d}y$, $I_3^{\beta_0} = (-2\pi/\beta_0)\int_S \Lambda_3^{\beta_0}\ \mathrm{d}x\,\mathrm{d}y$, and $I_4^{\beta_0} = (-2\pi/\beta_0)\int_S \Lambda_4^{\beta_0}\ \mathrm{d}x\,\mathrm{d}y$. The reader is additionally referred to Casacuberta *et al.* [41] for further details and interpretation on this decomposition of production. The evolution in x of $(-2\pi/\beta_0)\Lambda_{\beta_0}$ and $(-2\pi/\beta_0)\Lambda_m^{\beta_0}$, $m = 1$–4, both probed at $y = \tilde{y}^{\psi,\mathrm{str}}_{(0,1)}$, is shown in Fig. 5. The probing coordinate corresponds to the wall-normal location of the *core* of the streaks, i.e., linked to the secondary peak in the perturbation shape $|\tilde{\psi}|_{(0,1)}$ at the step [see small magenta circles in Fig. 3(a)]. Inspection of the spatial evolution of terms $(-2\pi/\beta_0)\Lambda_m^{\beta_0}$, $m = 1$–4, provides insight into the location and *strength* of the associated mechanisms. Their sign informs whether kinetic energy is transferred from the base flow to the perturbation field, $(-2\pi/\beta_0)\Lambda_m^{\beta_0} > 0$, or vice versa, $(-2\pi/\beta_0)\Lambda_m^{\beta_0} < 0$. This applies identically to production itself, $(-2\pi/\beta_0)\Lambda_{\beta_0}$ [Eq. (12)].

Figure 5 shows that production grows rapidly in x close downstream of the step, where the streaks first appear (see thick solid black line), and reveals that the increase of production is driven mainly by $I_2^{\beta_0}$ (see dashed red line), i.e., the lift-up effect. To elaborate further on this dominant role played by the mechanism of $I_2^{\beta_0}$, Fig. 6(a) additionally illustrates the spatial organization of its integrand [Eq. (16)] superimposed on the projected base-flow streamlines in the x-y plane. The corresponding

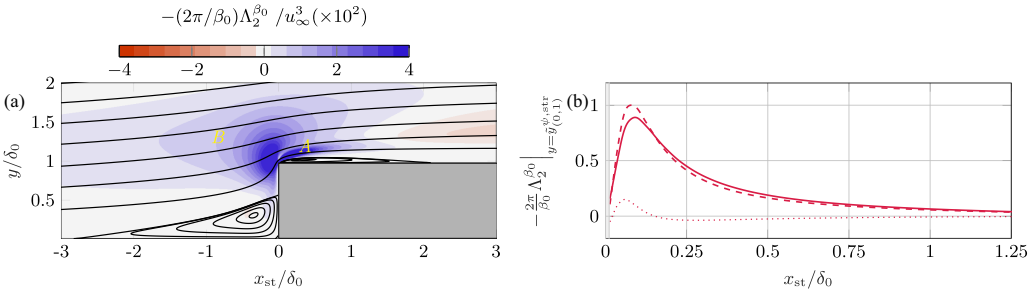

FIG. 6. Spatial evolution of $(-2\pi/\beta_0)\Lambda_2^{\beta_0}$ [Eq. (16)] with cross-sectional streamlines of the base flow (a) and chordwise evolution of individual terms of Eq. (16) at the wall-normal location of the core of the streaks (b): $(-2\pi/\beta_0)\kappa_2^{\beta_0}$ [solid, see Eq. (20)], remainder (dotted), global term $(-2\pi/\beta_0)\Lambda_2^{\beta_0}$ (dashed). All curves are normalized relative to maximum $\Lambda_2^{\beta_0}$.

three-dimensional organization of streamlines at the step is depicted in Casacuberta *et al.* [2, cf. Fig. 7(b)]. Two main destabilizing flow regimes [$(-2\pi/\beta_0)\,\Lambda_2^{\beta_0} > 0$] develop at the step; see labels "A" and "B" in Fig. 6(a). Regime "A" is associated to the new near-wall streaks incepted close downstream of the step, while regime "B" is mainly linked to the amplification of the incoming CFI as it approaches the step.

In regime "A" of Fig. 6(a), the term

$$\kappa_2^{\beta_0} = \left(\tilde{v}_{t,(0,1)}^{1}\tilde{v}_{n,(0,1)}^{2\,\dagger} + \text{c.c.}\right)\frac{\partial u_{\rm B}}{\partial y} \tag{20}$$

is the main contribution to $\Lambda_2^{\beta_0}$ in Eq. (16) and thus *drives* the action of the lift-up effect, as quantitatively demonstrated in Fig. 6(b) evaluating individual terms of Eq. (16) at $y = \tilde{y}_{(0,1)}^{\psi,\rm str}$. The term $\kappa_2^{\beta_0}$ may be interpreted as the vertical (i.e., pointing in y) perturbation by the cross-stream pattern ($\boldsymbol{v}_n'$) acting on the base-flow shear $\partial u_{\rm B}/\partial y$ and feeding growth to the streamwise-velocity perturbation ($\boldsymbol{v}_t'$) in x. The dominant influence of $\kappa_2^{\beta_0}$ reconciles with the perturbation behavior at the step (see Fig. 2), when it is examined through a classic wall-oriented perturbation decomposition [Eq. (8)]. That is, the component parallel to the wall and aligned with x, $u_{(0,1)}'$, manifests more prominently than the component aligned with z, $w_{(0,1)}'$ (Fig. 2). The resulting streaks at the step are initially aligned with the x direction, because the lift-up effect favors the amplification of the streamwise-oriented perturbation component [26] and the base-flow streamlines at the step undergo strong spanwise modulation [4,5] and bend vigorously towards the x direction; see Casacuberta *et al.* [2, cf. Figs. 7(b) and 7(d)].

Finally, it is instructive to visualize the arrangement of streaks at the step induced by the lift-up effect as shown in Fig. 7. Specifically, Fig. 7 illustrates the perturbation organization in y-z planes in the step (top) and no-step (bottom) cases at same (increasing) x positions. Figure 8 complements Fig. 7 by adding the unperturbed base flow, $||\boldsymbol{v}_{\rm B}|| + (\tau_{(0,1)}' + \tau_{(0,1)}'^{\,\dagger})$, where $||\boldsymbol{v}_{\rm B}||$ is the modulus of the local base-flow vector. In short, Fig. 8 expresses the velocity of the steady developed flow [Eq. (1)] in the local streamline direction. In the presence of the step, the incoming crossflow vortices lift off the wall as they approach the step in x. In a perturbation sense, the highly energetic $\boldsymbol{v}_t'$ structures correspondingly shift upward significantly in the upstream vicinity of the step; see color contours in Fig. 7(a) representing $x_{\rm st}/\delta_0 = -0.02$, when compared to reference conditions [Fig. 7(e)]. Note that Fig. 7 illustrates the modulus of $\boldsymbol{v}_t'$, namely, τ'. However, the cross-stream perturbation pattern $\boldsymbol{v}_n'$ maintains a dominant contribution at a similar location to reference conditions, i.e., at approximately $y/\delta_0 \approx 1$. The *strength* of $\boldsymbol{v}_n'$ is characterized by the length of white arrows in Figs. 7(a) and 7(e). At the same time, the base flow at the step is highly sheared; see Casacuberta *et al.* [2] (cf. Fig. 6). This combination of effects sets the conditions

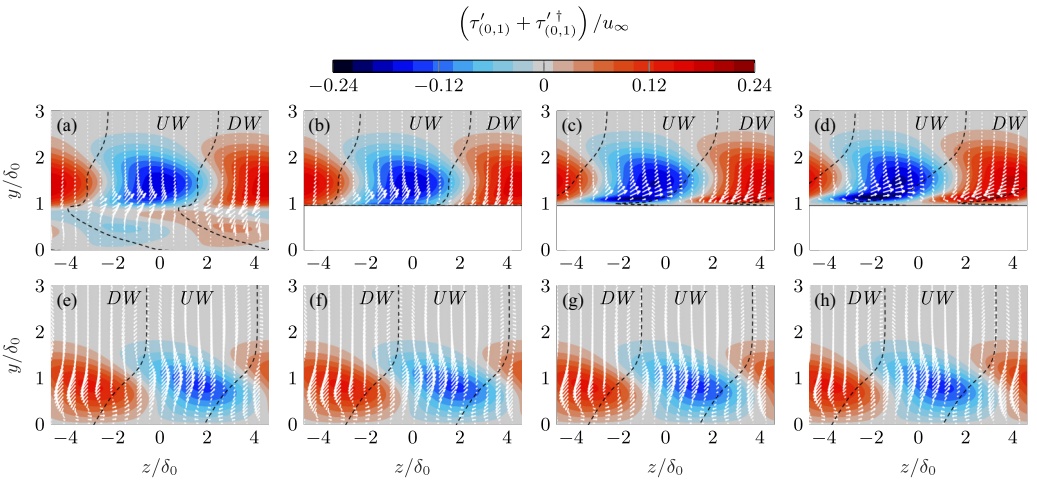

FIG. 7. Streamwise-velocity perturbation (color contour) in y-z planes for the step (top) and reference no-step (bottom) cases at -0.02 [(a), (e)], 0.04 [(b), (f)], 0.52 [(c), (g)], 1 [(d), (h)]. In-plane organization of the cross-stream-velocity perturbation (white arrows). Dashed lines segregate cross-stream-perturbation upwash (UW) and downwash (DW).

for the *weak* cross-stream perturbation to effectively displace low-momentum fluid upward and high-momentum fluid downward at the upper step corner and thus give rise to rapidly amplified streamwise streaks of alternating sign in z [Figs. 7(b)–7(d)]. Specifically in unswept (i.e., two-dimensional) forward-facing-step flow in a channel, Wilhelm *et al.* [23] similarly report that even very small incoming perturbations, namely, less than 1% of the mean-flow velocity, produce noticeable streaky structures at the step. The multiple similarities between both studies suggests that the streaks are a linear perturbation of forward-facing-step flow that develops as a *sensitive reaction to incoming perturbations* [23].

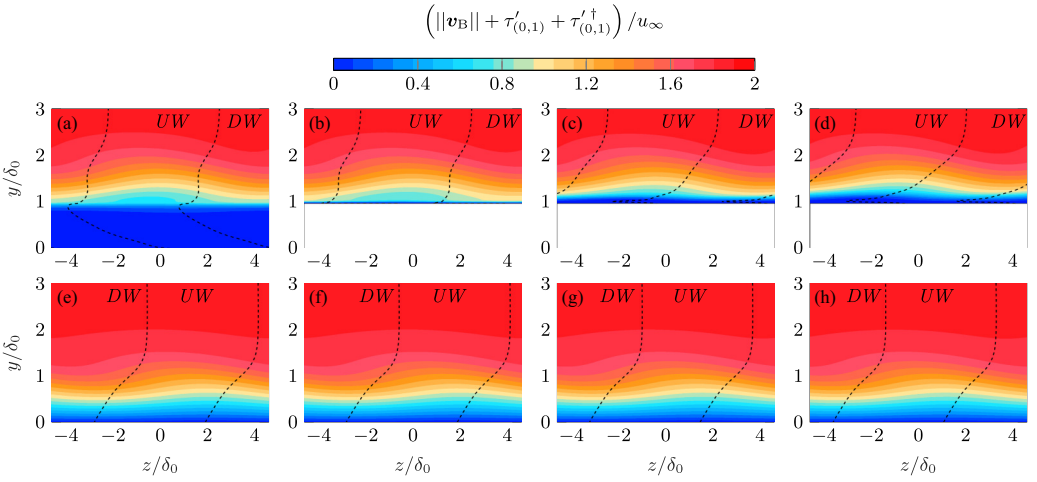

FIG. 8. Steady total streamwise flow (color contour), in y-z planes for the step (top) and reference no-step (bottom) cases at -0.02 [(a), (e)], 0.04 [(b), (f)], 0.52 [(c), (g)], 1 [(d), (h)]. Dashed lines segregate cross-stream-perturbation upwash (UW) and downwash (DW); see Fig. 7 for reference.

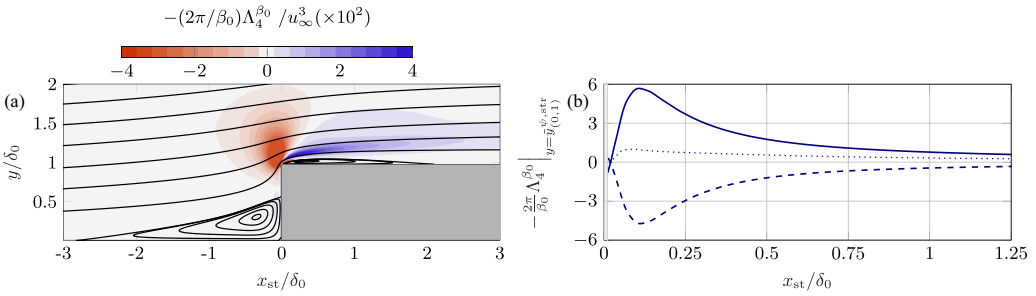

FIG. 9. Spatial evolution of $(-2\pi/\beta_0)\Lambda_4^{\beta_0}$ [Eq. (21)] with cross-sectional streamlines of the base flow (a) and chordwise evolution of individual terms of Eq. (21) at the wall-normal location of the core of the streaks (b): $(-2\pi/\beta_0)\chi_4^{\beta_0}$ (solid), sum of remainder (dashed), global term $(-2\pi/\beta_0)\Lambda_4^{\beta_0}$ (dotted). All curves are normalized relative to $\max(\Lambda_4^{\beta_0})$.

B. The role of the push-forward effect

The lift-up effect plays a pivotal role in the inception of streaks at the step. However, the results of Fig. 5 indicate that the push-forward mechanism, $I_4^{\beta_0}$ [Eq. (18)], contributes as well to energy production, P_{β_0} [Eq. (12)] at the streaks. Even more so, the contribution of $I_4^{\beta_0}$ (dotted blue in Fig. 5) surpasses that of $I_2^{\beta_0}$ (dashed red in Fig. 5) eventually in x. As previously mentioned, the mechanism of $I_4^{\beta_0}$ may be understood as a self-induction effect of the field $\boldsymbol{v}_t'$ onto itself. That is, the streamwise-velocity perturbation displaces base-flow momentum in the direction of the perturbation and hence inherits some of its energy.

This is expanded upon in the following manner: Fig. 9(a) depicts the spatial evolution of the integrand of $I_4^{\beta_0}$ [Eq. (18),] $(-2\pi/\beta_0)\Lambda_4^{\beta_0}$, with

$$\begin{aligned}\Lambda_4^{\beta_0} = {} & \big(\tilde{v}_t^1\ \tilde{v}_t^{1\dagger} + \text{c.c.}\big)\frac{\partial u_{\rm B}}{\partial x} + \big(\tilde{v}_t^1\ \tilde{v}_t^{2\dagger} + \text{c.c.}\big)\frac{\partial u_{\rm B}}{\partial y} + \big(\tilde{v}_t^2\ \tilde{v}_t^{1\dagger} + \text{c.c.}\big)\frac{\partial v_{\rm B}}{\partial x} \\ & + \big(\tilde{v}_t^2\ \tilde{v}_t^{2\dagger} + \text{c.c.}\big)\frac{\partial v_{\rm B}}{\partial y} + \big(\tilde{v}_t^3\ \tilde{v}_t^{1\dagger} + \text{c.c.}\big)\frac{\partial w_{\rm B}}{\partial x} + \big(\tilde{v}_t^3\ \tilde{v}_t^{2\dagger} + \text{c.c.}\big)\frac{\partial w_{\rm B}}{\partial y},\end{aligned} \tag{21}$$

where the subscript $(0,1)$ has been removed for conciseness. A prominent region of $(-2\pi/\beta_0)\ \Lambda_4^{\beta_0} > 0$ develops close downstream of the step [see Fig. 9(a)], and Fig. 9(b) quantitatively demonstrates that the term

$$\chi_4^{\beta_0} = \big(\tilde{v}_{t,(0,1)}^1 \tilde{v}_{t,(0,1)}^{1\dagger} + \text{c.c.}\big)\frac{\partial u_{\rm B}}{\partial x} = 2\big|\tilde{v}_{t,(0,1)}^1\big|^2\frac{\partial u_{\rm B}}{\partial x} \tag{22}$$

has the largest contribution to $I_4^{\beta_0}$ in this region. Based on the main criterion followed above, Fig. 9(b) evaluates individual terms of Eq. (21) at the wall-normal location of the streaks, i.e., at $y = \tilde{y}^{\psi,{\rm str}}_{(0,1)}$.

From Eq. (22) and the results of Fig. 9(b), it may be concluded that the stabilizing or destabilizing contribution of $I_4^{\beta_0}$ at the step is dictated essentially by whether the base-flow velocity $u_{\rm B}$ accelerates or decelerates in x. If the base flow decelerates, $\partial u_{\rm B}/\partial x < 0$, then $\chi_4^{\beta_0} < 0 \Rightarrow I_4^{\beta_0} > 0$, implying that kinetic energy is transferred from the base flow to the perturbation field and the process is locally destabilizing. The inverse holds true if the base flow accelerates in x, $\partial u_{\rm B}/\partial x > 0 \Rightarrow I_4^{\beta_0} < 0$. Casacuberta *et al.* [2] show that the pressure gradient around the step carries local flow acceleration $(\partial u_{\rm B}/\partial x > 0)$ close upstream of the step, which is immediately followed in x by local flow deceleration $(\partial u_{\rm B}/\partial x < 0)$ close downstream of the step. In conformity with this description, the mechanism of $I_4^{\beta_0}$ acts first stabilizing and then destabilizing as the perturbation ascends the step apex; see Fig. 9(a).

Following this rationale, the inception of energetic streamwise streaks just downstream of the step, embedded in a locally decelerating boundary layer in x, activates the mechanism of $I_4^{\beta_0}$. In combining the observations from Sec. IV A and the current section, the initial inception of near-wall streaks at the step is mainly ascribed to the lift-up effect, but their subsequent amplification in x appears to be driven by a combination of lift-up, $I_2^{\beta_0}$, and push-forward, $I_4^{\beta_0}$. Lanzerstorfer and Kuhlmann [19] report as well a non-negligible contribution of $I_4^{\beta_0}$ on streaks in unswept forward-facing-step flow albeit with a major difference noted with the present work. In the aforementioned work, the authors state that the perturbation streaks are self-sustained by a feedback of the recirculating flow on the upper wall of the step. In the present case, while recirculating flow is present at the step as well [2], the streaks are sustained by a preexisting CFI influencing the step flow.

C. Modal and nonmodal growth of streaks at the step

This section examines whether the presently discussed near-wall streaks that form at the step are the result of modal or nonmodal instability. It is well established that nonmodal growth driven by the lift-up effect typically manifests as rapidly formed streamwise streaks. However, the lift-up effect plays a role as well in other perturbation systems such as Görtler instability; see the discussion by Marxen *et al.* [26]. As noted by Floryan and Saric [71] and Floryan [68], Görtler instability exhibits a *very weak cellular motion* in the cross-stream plane, where the streamwise-velocity perturbation correspondingly originates from a *defect in the mean flow* due to the convection of streamwise momentum by the cross-stream vortex-like motion.

In previous work, Görtler instability has been suggested as the mechanism behind near-wall streaky structures in two-dimensional [20] and three-dimensional [16], forward-facing-step flow. Next to it, an instability of inflectional crossflow type [4] and spatial nonmodal growth are additional candidates for the amplification of streaky structures at the step. To segregate between modal and nonmodal effects at the step, the methodology of Marxen *et al.* [26] is followed in this section. Marxen *et al.* [26] decompose the velocity-perturbation vector into components tangential and normal to the local orientation of base-flow streamlines; that is, the velocity-perturbation vector is decomposed in the local streamwise and cross-stream directions, as formulated in Eq. (9) in this work. In the case of purely modal growth, all velocity components ought to display a similar spatial growth rate, implying the existence of a single (growing or decaying) perturbation *eigenmode* [26]. It is noted that in nonparallel flow this can only be attained approximately, inasmuch as the different velocity components corresponding to a modal instability mechanisms display minor differences; see Saric [72], Bertolotti *et al.* [60, cf. Sec. 4.1], and Gaster [73]. However, in the case of nonmodal growth by the lift-up effect, the amplification of the streamwise-aligned perturbation component is significantly favored over its cross-stream counterpart, and the growth rate of one component can be an order of magnitude larger than another, or even of opposite sign (i.e., one component growing while the other component decays).

The evolution of perturbation growth rates [Eq. (3)] in x in the near-wall step flow is illustrated in Fig. 10. Red circles characterize the growth rate of the streamwise-velocity perturbation, $\boldsymbol{v}'_{t,(0,1)}$, based on the amplitude function $|\tilde{\tau}|_{(0,1)}$ (Sec. III C), and black triangles characterize the growth rate of the perturbation vector itself, $\boldsymbol{v}'_{(0,1)}$, based on the amplitude function $|\tilde{\psi}|_{(0,1)}$ [Eq. (6)]. Both amplitude functions are measured at a common wall-normal position associated to the streaks, $y = \tilde{y}^{\psi,\mathrm{str}}_{(0,1)}$ (Sec. III B). Initially from $x_{\mathrm{st}} = 0$, i.e., the step corner where the streaks are first incepted, the evolution of growth rates in Fig. 10 differs considerably. The significantly larger spatial growth rate (in absolute value) of $\boldsymbol{v}'_{t,(0,1)}$, when compared to $\boldsymbol{v}'_{(0,1)}$, implies that growth of streamwise perturbations is favored over cross-stream perturbations. Following the discussion of Marxen *et al.* [26], this is an imprint of spatial nonmodal growth produced by the convection of streamwise momentum in the cross-stream plane through *lift up* (Sec. IV A), which cannot be described by an individual perturbation eigenmode inherent to the step-flow profiles in this case. The growth

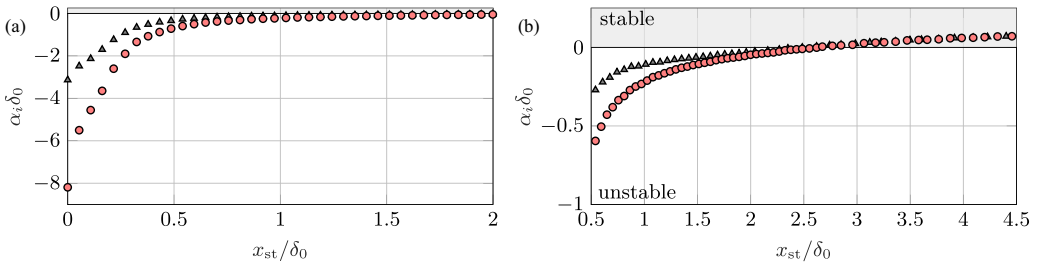

FIG. 10. Spatial growth rates of the total, $|\tilde{\psi}|_{(0,1)}$ (triangles), and streamwise, $|\tilde{\tau}|_{(0,1)}$ (circles), perturbations at the wall-normal location of streaks, $y = \tilde{y}^{\psi,\mathrm{str}}_{(0,1)}$, in the ranges $0 \leqslant x_{st}/\delta_0 \leqslant 2$ (a) and $0.5 \leqslant x_{st}/\delta_0 \leqslant 4.5$ (b).

rate of the streamwise-velocity perturbation being larger than that of the perturbation itself in turn implies that the cross-stream perturbation decays in space while inducing the streamwise streaks at the step.

D. Coexistence of high-order harmonic streaks at the step

The main discussion above has revolved around analysis of the fundamental streaks. However, the results from DNS show that the streaks of fundamental wave number, $\beta = \beta_0$, actually coexist at the step with streaks of high-order harmonic wave number, $\beta > \beta_0$. The origin of the latter is discussed in this section.

In the Baseline case (Table I), a stationary crossflow eigenmode with $\beta = \beta_0$ is prescribed at the inflow. Gradually in x, high-order harmonic components of the crossflow perturbation with $\beta = j\beta_0$, $j = 2, \ldots, N$ amplify spatially due to nonlinear perturbation interactions. When approaching the step in x, all incoming harmonics lift off the wall and pass over the step. Near-wall velocity-perturbation streaks are induced locally at the upper step corner, which manifest at spanwise perturbation wave numbers of $\beta = j\beta_0$, $j = 2, \ldots, N$, hence they are contained in each spanwise perturbation mode [Eq. (2)]. This organization of streaks was illustrated in Fig. 2(a) for mode $\beta = \beta_0$, and it is here depicted for mode $\beta = 2\beta_0$ in Fig. 11; the latter is representative of the behavior of perturbations with $\beta > 2\beta_0$.

Next, the methodology of Sec. IV A characterizing the lift-up effect is reproduced for streaks with $\beta > \beta_0$. It is found that the production terms $I_2^{j\beta_0}$ add the dominant energy contribution (vs $I_1^{j\beta_0}$, $I_3^{j\beta_0}$, $I_4^{j\beta_0}$) for all high-order harmonic perturbation fields, $\boldsymbol{v}'_{(0,j)}$ with $j \geqslant 2$. Inspection of the flow organization reveals that, similarly to the fundamental mode, the cross-stream pattern $\boldsymbol{v}'_{n,(0,j)}$ of each incoming high-order perturbation mode displaces low-momentum fluid upward and

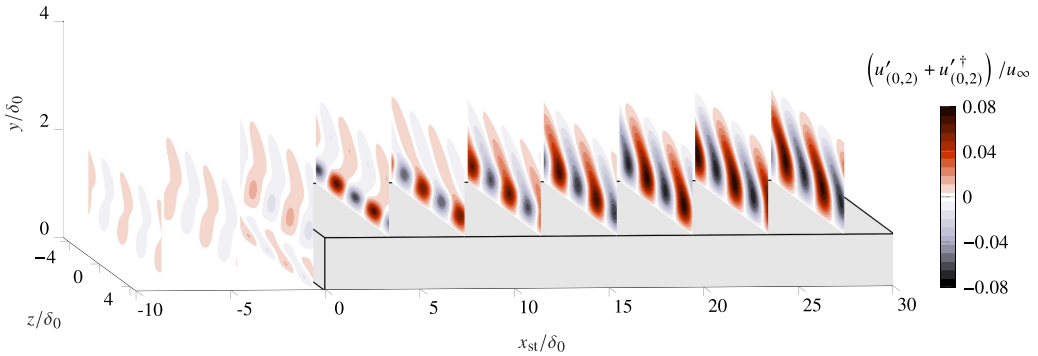

FIG. 11. Organization of the chordwise velocity-perturbation field for $\beta = 2\beta_0$.

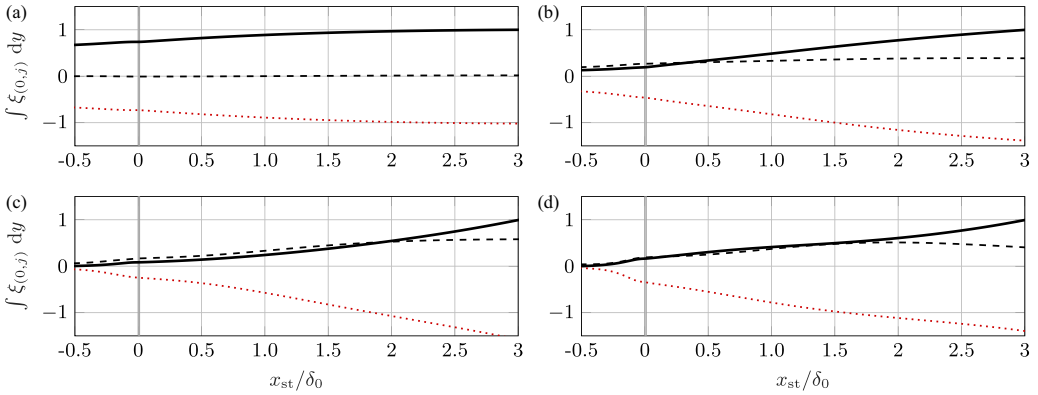

FIG. 12. Chordwise evolution of integral budget terms of the energy-balance equations of the spanwise-harmonic perturbation modes: ξ identifies linear production (solid black), the work of nonlinear interactions (dashed black), and the remainder of linear mechanisms (dotted red) for the stationary perturbation modes $j = 1$ (a), 2 (b), 3 (c), and 4 (d). All curves are normalized relative to the maximum of linear production in each subplot.

high-momentum fluid downward on interaction with the step flow. Consequently, spanwise-alternating regions of streamwise-momentum deficit and excess form near the wall in a short span of space, which manifest as rapidly-formed streamwise streaks in the corresponding field $\boldsymbol{v}'_{t,(0,j)}$.

In conclusion, if multiple harmonic stationary perturbations coexist upstream of the step, then corresponding streaky structures will be induced at the step at respective spanwise wavelengths. The streak formation appears to be governed linearly for each incoming mode, individually. To be noted, the initial spanwise phase of the newly formed streaks is inherently set by the modal nonlinear arrangement of harmonic modes upstream of the step. The mechanisms governing the higher harmonics are highlighted by Figs. 12(b)–12(d) quantifying the integral evolution of kinetic-energy transfer of the stationary perturbation modes following the approach of Casacuberta *et al.* [69]. The integration domain extends up to $y/\delta_0 = 1.5$. In line with the main discussion above, the behavior of the fundamental streaks is fully linearly dominated at the step [Fig. 12(a)]. When moving downstream, subsequent nonlinear interaction among the fundamental and high-order harmonic streaky structures of comparable or larger magnitude than the linear production is not to be discarded but is not further addressed in this work.

V. EFFECTS OF SPANWISE VELOCITY AND SPANWISE PERTURBATION WAVE NUMBER

A. Effect of spanwise velocity

The discussion in the previous sections has explored the origin and nonmodality of the streaks. A heuristic experiment is performed next to further confirm that the streaks at the step cannot be supported as (modal) CFI of the inflectional step-flow profiles. The input parameter w_∞/u_∞ (Sec. II B), which is proportional to the global sweep angle governing the flow, is increased gradually in small steps of Δw_∞ for fixed u_∞; see Sec. II B for details on the tested free-stream conditions and the preimposed boundary-layer perturbation. For a purely two-dimensional base flow, $w_\infty/u_\infty = 0$, the crossflow-velocity profile vanishes. In this scenario CFI is not tenable, and thus, if streaks manifest, they may not be ascribed to CFI. The flow cases discussed in this section are labeled as Test A–F in Table I.

The organization of the perturbation field at the step is shown in Fig. 13 for decreasing $|w_\infty/u_\infty|$ (top to bottom). The planes in the top row illustrate Test A in Table I, $\max(|w_\infty/u_\infty|)$, which corresponds identically to the free-stream conditions of the main case discussed in Secs. III and IV. The planes in the bottom row characterize Test F in Table I, $w_\infty/u_\infty = 0$, which corresponds

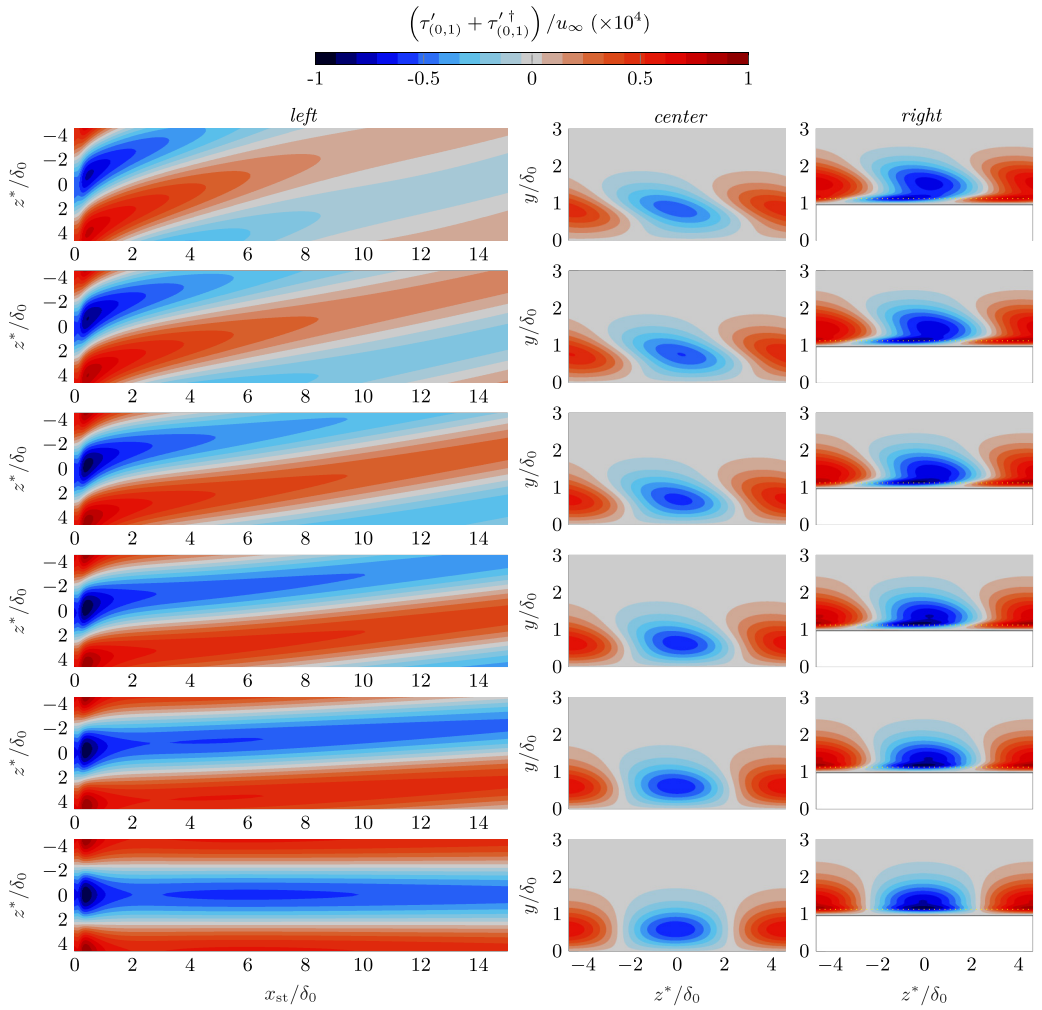

FIG. 13. Evolution of perturbation streaks at $y/\delta_0 = 1.12$ (left) and in y-z planes upstream of the step, $x_{st}/\delta_0 = -10$ (center), and downstream of the step, $x_{st}/\delta_0 = 1$ (right). Top to bottom illustrates streamwise-velocity perturbation as color contour from case $\max(|w_\infty/u_\infty|)$ (Test A) to case $w_\infty/u_\infty = 0$ (Test F) following Table I. Dotted horizontal yellow line is the wall-normal location of the x-z plane and the coordinate z^* indicates spanwise shift for centered low-speed streak.

to a purely two-dimensional base flow. The results of Fig. 13 (left and right) highlight that a region of additional perturbation amplification at the upper step corner manifests in all cases. Figure 13 (center) additionally depicts the perturbation field upstream of the step for reference. The corresponding three-dimensional organization of the perturbation planes of Fig. 13 is shown in Figs. 16 and 17 in the Appendix. Overall, these results confirm the universal existence and structural similarities of stationary perturbation streaks at the step for the full range of tested spanwise velocities. Streaks manifest in unswept and low-sweep-angle conditions, hence evidence is provided that they are not an additional (modal) crossflow instability.

B. Effect of spanwise wave number

The choice of spanwise perturbation wavelength in this work, $\lambda_z = 2\pi/\beta_0 = 7.5$ mm (Sec. II), yields the largest (linear) amplification factor of the stationary crossflow perturbation at the end of

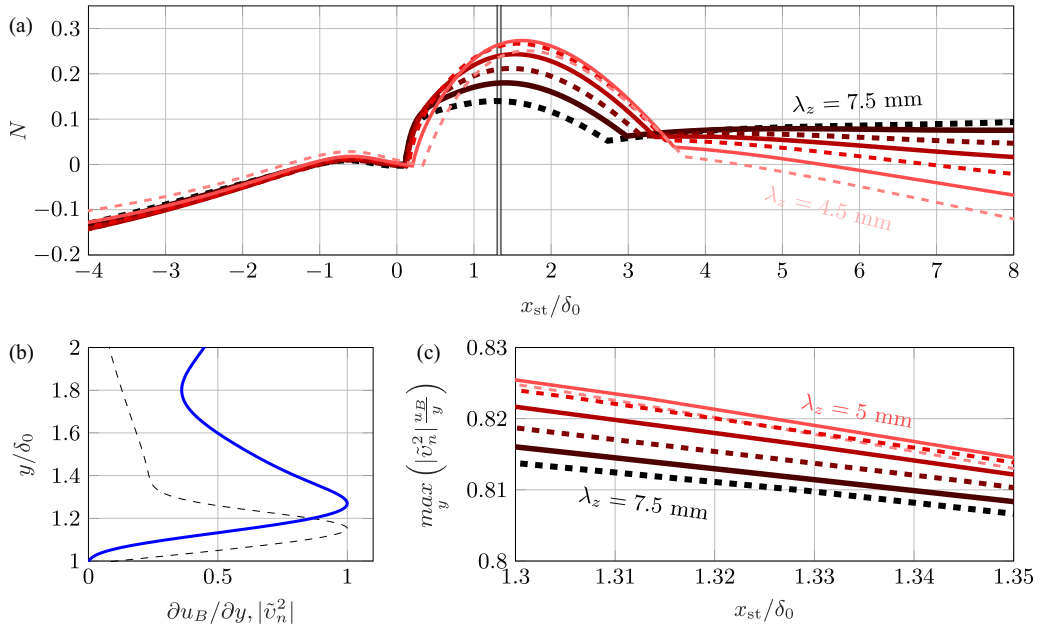

FIG. 14. Evolution in x of the perturbation amplification factor [Eq. (23)] computed with AHLNS on the swept base flow with $w_\infty/u_\infty = -1.241$ (Table I) for $\lambda_z \in [4.5, 7.5]$ mm, in steps of $\Delta\lambda_z = 0.5$ mm: thin-to-thick (and bright-to-dark) line style illustrates increasing λ_z (a). Normalized profiles of $|\tilde{v}_n^2|$ (solid blue) and $\partial u_B/\partial y$ (dashed black) for $\lambda_z = 5$ mm at $x_{st}/\delta_0 = 1.3$ (b). Evolution in x of the maximum along y of the correlation between $|\tilde{v}_n^2|$ and $\partial u_B/\partial y$ (c). Solid vertical lines in (a) indicate $1.3 \leqslant x_{st}/\delta_0 \leqslant 1.35$.

the domain in reference conditions. However, there is no reason to assume, *a priori*, that this value yields as well the largest amplification factor of streaks at the step. As such, this section analyzes the effect of spanwise wavelength on streaks at the step.

A parametric study using linear stability analysis on the swept base flow with $w_\infty/u_\infty = -1.241$ (Table I) has been carried out with (AL)HNS (see Sec. II D) to identify most critically amplified streaks in relation to the wavelength of upstream-existing perturbation modes. A range of input perturbation wavelengths is tested, namely, $\lambda_z \in [4.5, 7.5]$ mm, in steps of $\Delta\lambda_z = 0.5$ mm. Figure 14 depicts perturbation amplification factors in x evaluated as

$$N(x, \lambda_z) = N^\star(x, \lambda_z) - N^\star(x_{str}, \lambda_z) \tag{23}$$

with

$$N^\star(x, \lambda_z) = \ln\left(\frac{|\tilde{u}|^{max}_{(0,1)}(x, \lambda_z)}{|\tilde{u}|^{max}_{(0,1)}(0, \lambda_z)} \right) \tag{24}$$

and x_{str} denoting the x position where the amplitude of near-wall streaks surpasses that of CFI developing above. Considering the discussion of Sec. III B on amplitude definitions, amplitude of the near-wall streaks in Fig. 14(a) is monitored approximately in the range $0 \leqslant x_{st} \leqslant 4$. Downstream of it, the measure of amplitude characterizes CFI.

The results of Fig. 14(a) indicate that the maximum amplification factor of streaks is attained for $\lambda_z = 5$ mm. For reference, this value is more than six times the step height. Following the main discussion above, the differences in amplification factor of streaks at the step [Fig. 14(a)] can be linked to a measure of *growth efficiency* of the incoming perturbation pattern. Here the term growth efficiency expresses the sense of correlation between the profiles (i.e., the shape along y) of the incoming cross-stream perturbation component and the base-flow shears; the *most efficient*

interaction between these two agents will induce the largest spatial transient growth of kinetic perturbation energy locally downstream of the step. This concept shares the same foundations as *optimal* perturbations [28,35,36,74]. However, in the present case, the set of possible initial perturbations is bounded and given by the shape of each considered spanwise wavelength of the preexisting perturbation in the incoming stream. This effect is here quantified through the term $\kappa_2^{\beta_0}$ [Eq. (20)], which was shown above to add the main contribution to the lift-up effect at the step [Fig. 6(b)]. Following the mathematical definition of $\kappa_2^{\beta_0}$ (Sec. IV A), it is identified that the normal perturbation shape $|\tilde{v}_n^2|$ (Sec. III C) and the base-flow shear $\partial u_B/\partial y$ yield maximum correlation for $\lambda_z = 5$ mm. This implies that, the product between the profiles of $|\tilde{v}_n^2|$ and $\partial u_B/\partial y$ [see Fig. 14(b)] at a representative x position produces a profile whose peak attains maximum strength for $\lambda_z = 5$ mm. The latter is quantitatively characterized in Fig. 14(c) considering $x_{st}/\delta_0 \approx 1.3$, i.e., close upstream of the point of maximum amplification of the smaller-wavelength streaks.

VI. CONCLUSIONS

In the past three decades, several investigations have reported the ubiquitous presence of streaky structures in two-dimensional [19,22–24] and three-dimensional [2] laminar forward-facing-step flow. In the latter case, which is the scope of this work, the step is immersed in swept-wing boundary-layer flow, and a classic stationary crossflow instability preexists upstream of the step. The isolation of stationary velocity-perturbation streaks [2] in a structural sense reconciles well with recent reports of significant perturbation amplification at the upper step corner [3–5,16]. Notwithstanding the potential role of the streaks in promoting laminar-turbulent transition of swept-wing flow [6], there is no definite consensus in the literature regarding the mechanisms of instability growth giving rise to the streaks. In this work, direct numerical simulations have been performed to scrutinize the stationary velocity-perturbation streaks that form close downstream of two-dimensional forward-facing step of fixed height embedded in laminar incompressible swept-wing boundary-layer flow.

The streaks appear as alternating regions of streamise-velocity excess and deficit distributed along the step-edge direction and they develop spatially very close to the wall. A linear nonmodal growth mechanism attributed to the lift-up effect is shown to be mainly responsible for the local inception of the streaks at the upper step corner. It has been isolated that the cross-stream pattern of the fundamental (i.e., primary-wavelength) stationary crossflow perturbation in the incoming boundary layer *lifts-up* and pushes down low- and high-momentum fluid in adjacent regions of the highly sheared step flow. Under this principle, the lift-up effect gives rise to rapidly amplified and highly energetic streamwise streaks that inherently adopt the spanwise wavelength of the incoming boundary-layer perturbation. This has been argued by decomposing the perturbation field into components tangential (i.e., streamwise-aligned) and orthogonal (i.e., cross-stream-aligned) to the local orientation of base-flow streamlines and examining the mechanism of perturbation production, that is, the production term of the Reynolds-Orr equation. The analysis has revealed that a mechanism of base-flow deceleration, essentially a self-induction effect of streamwise perturbations, additionally contributes to feeding growth to the streaks in a region further downstream of the step.

The results of this work suggest that a wide range of incoming three-dimensional stationary perturbations have the potential to trigger structurally similar stationary near-wall streaks at the step. A key ingredient is the ability of the incoming three-dimensional cross-stream perturbation pattern to effectively redistribute base-flow momentum on interaction with the step flow. As such, the results of this work reconcile well with the main conclusions of Lanzerstorfer and Kuhlmann [19] for their study of two-dimensional step flow. Namely, the lift-up effect is primarily responsible for the inception of streaks at the step. In turn, the streaks are a linear perturbation that develops as a *sensitive reaction of the flow* to three-dimensional perturbations in the incoming boundary layer. This is further supported by the conclusions of Wilhelm *et al.* [23]. The present work establishes that the streaks are not a manifestation of additional crossflow instability of the distorted step-flow profiles, as suggested by other studies.

Finally, linear stability analysis performed through the harmonic Navier-Stokes (HNS) method has confirmed that the streaks are a linear perturbation of forward-facing-step flow. The efficiency of the HNS class of computations allows for parametric studies of critical instability specifications. In this work, effects of spanwise wavelength have been assessed. Within the limits of the present parametric study, perturbation streaks universally form at the step independently of the wavelength of incoming boundary-layer perturbations, albeit the streaks exhibit different spatial amplification factors. An analysis of spanwise-velocity effects, i.e., representative of sweep-angle conditions, has similarly illustrated that stationary streaks form at the step independently of the local organization of the flow. The present work supports the universality of stationary perturbation streaks in three-dimensional laminar forward-facing-step flow, whose main structural features and initial amplitude are set by pertinent stationary three-dimensional perturbations in the incoming boundary layer.

ACKNOWLEDGMENTS

This work has received HPC resources from the Dutch national e-infrastructure with the support of SURF Cooperative. J.C. and M.K. acknowledge the support of the European Research Council through Starting Grant No. 803082 GloWing. Moreover, the authors express their gratitude to Dr. A. F. Rius-Vidales, Dr. Giulia Zoppini, and Marina Barahona for fruitful discussions on the topic.

APPENDIX: PERTURBATION ORGANIZATION

This section provides additional plots of perturbation organization. Figures 15, 16, and 17 complement the description of perturbation fields presented in Secs. III C and V A.

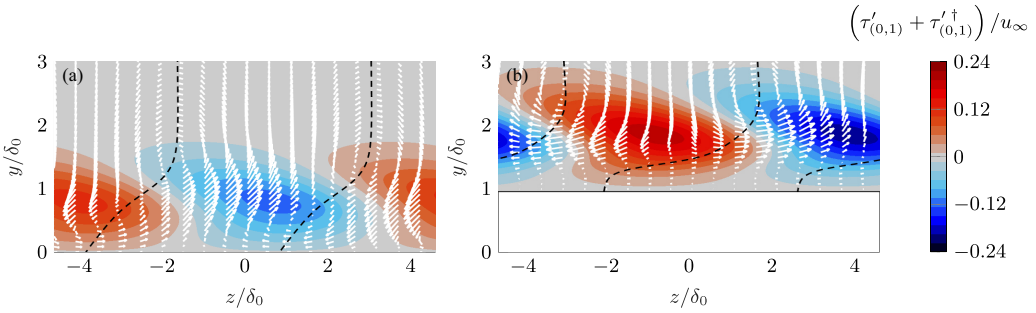

FIG. 15. Organization of streamwise-velocity (color contour) and in-plane cross-stream-velocity (white arrows) perturbations in y-z planes upstream, $x_{st}/\delta_0 = -10$(a), and downstream, $x_{st}/\delta_0 = 20$(b), of the step in case Baseline of Table I. Dashed black lines segregate cross-stream-perturbation upwash and downwash.

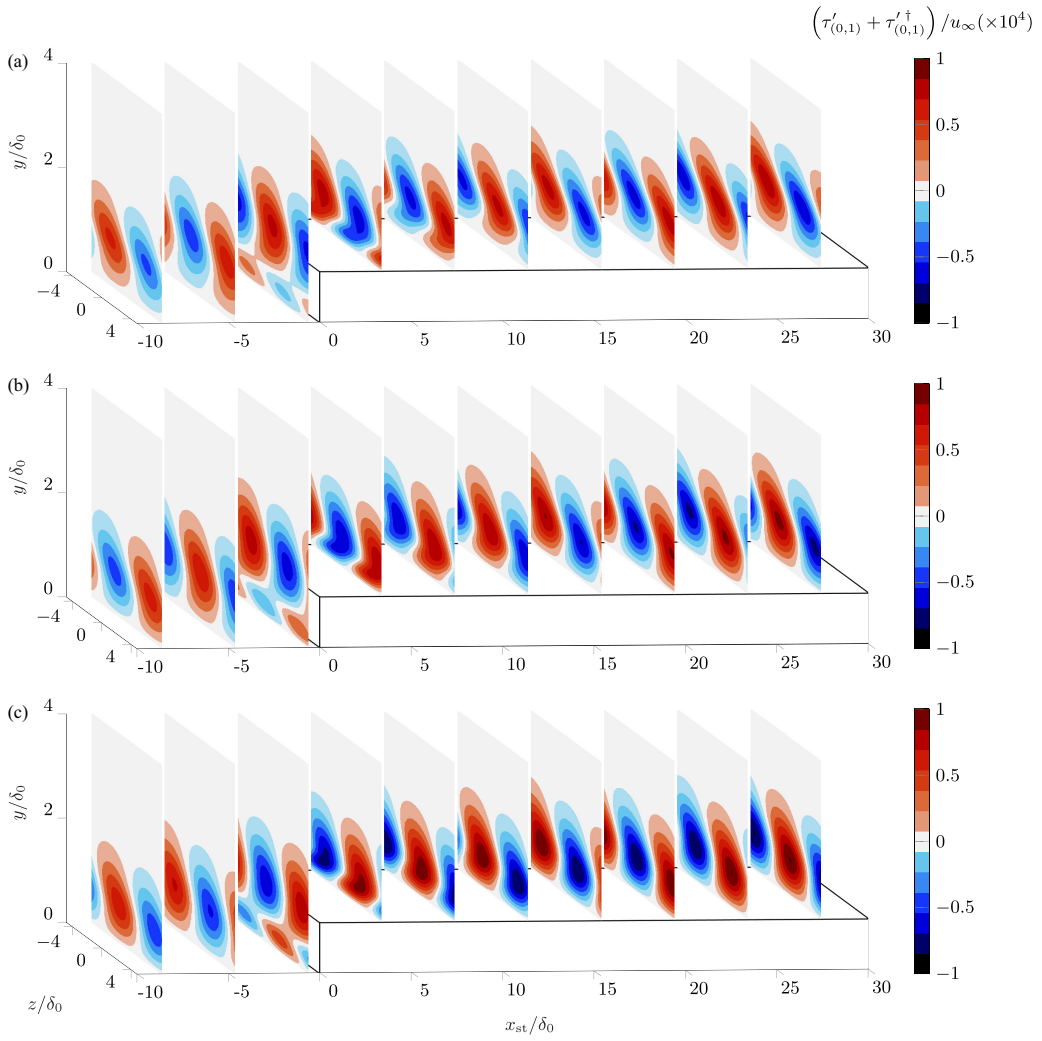

FIG. 16. Organization of the streamwise-velocity perturbation for $\beta = \beta_0$ in cases Test A (a), B (b), and C (c) of Table I.

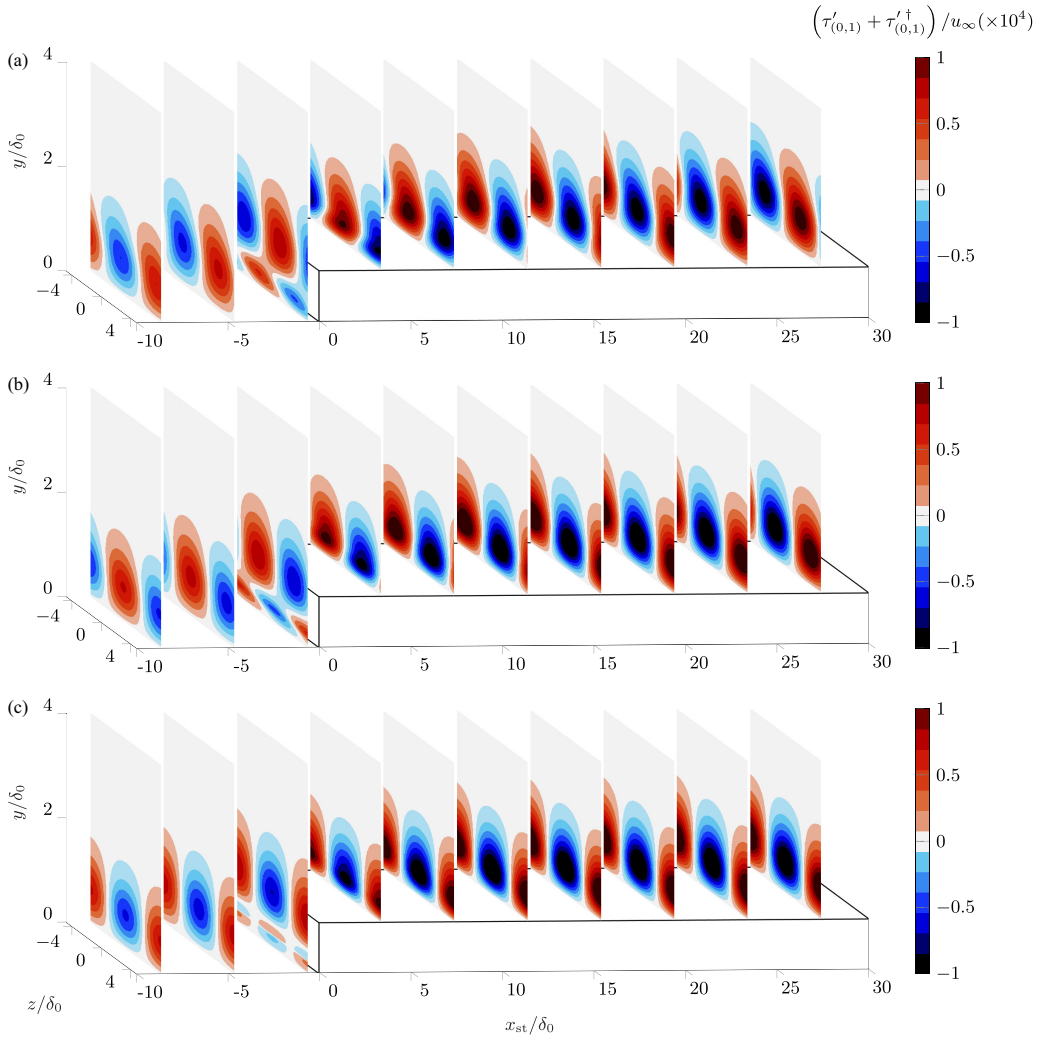

FIG. 17. Organization of the streamwise-velocity perturbation for $\beta = \beta_0$ in cases Test D (a), E (b), and F (c) of Table I.

[1] J. Casacuberta, S. Hickel, and M. Kotsonis, Mechanisms of interaction between stationary crossflow instabilities and forward-facing steps, AIAA Paper 2021-0854 (2021).

[2] J. Casacuberta, S. Hickel, S. Westerbeek, and M. Kotsonis, Direct numerical simulation of interaction between a stationary crossflow instability and forward-facing steps, J. Fluid Mech. **943**, A46 (2022).

[3] M. W. Tufts, H. L. Reed, B. K. Crawford, G. T. Duncan Jr., and W. S. Saric, Computational investigation of step excrescence sensitivity in a swept-wing boundary layer, J. Aircr. **54**, 602 (2017).

[4] J. L. Eppink, Mechanisms of stationary cross-flow instability growth and breakdown induced by forward-facing steps, J. Fluid Mech. **897**, A15 (2020).

[5] A. F. Rius-Vidales and M. Kotsonis, Impact of a forward-facing step on the development of crossflow instability, J. Fluid Mech. **924**, A34 (2021).

[6] J. Casacuberta, S. Hickel, and M. Kotsonis, Laminar-turbulent transition in swept-wing flows with a supercritical forward-facing step, in *ERCOFTAC Workshop Direct and Large Eddy Simulation* (Springer Nature, Cham, 2023), pp. 151–156.

[7] L. Mack, Special Course on Stability and Transition on Laminar Flows, AGARD Report No. 709 (1984).
[8] D. Arnal, Special Course on Progress in Transition Modelling, AGARD Report No. 793 (1993).
[9] W. S. Saric, H. L. Reed, and E. B. White, Stability and transition of three-dimensional boundary layers, Annu. Rev. Fluid Mech. **35**, 413 (2003).
[10] H. Deyhle and H. Bippes, Disturbance growth in an unstable three-dimensional boundary layer and its dependence on environmental conditions, J. Fluid Mech. **316**, 73 (1996).
[11] M. R. Malik, F. Li, M. M. Choudhari, and C.-L. Chang, Secondary instability of crossflow vortices and swept-wing boundary-layer transition, J. Fluid Mech. **399**, 85 (1999).
[12] W. Koch, F. P. Bertolloti, A. Stolte, and S. Hein, Nonlinear equilibrium solutions in a three-dimensional boundary layer and their secondary instability, J. Fluid Mech. **406**, 131 (2000).
[13] P. Wassermann and M. Kloker, Mechanisms and passive control of crossflow-vortex-induced transition in a three-dimensional boundary layer, J. Fluid Mech. **456**, 49 (2002).
[14] J. Serpieri and M. Kotsonis, Three-dimensional organisation of primary and secondary crossflow instability, J. Fluid Mech. **799**, 200 (2016).
[15] H. Bippes, Basic experiments on transition in the three-dimensional boundary layers dominated by crossflow instability, Prog. Aerosp. Sci. **35**, 363 (1999).
[16] A. F. Rius-Vidales and M. Kotsonis, Unsteady interaction of crossflow instability with a forward-facing step, J. Fluid Mech. **939**, A19 (2022).
[17] A. F. Rius-Vidales and M. Kotsonis, Influence of a forward-facing step surface irregularity on swept wing transition, AIAA J. **58**, 5243 (2020).
[18] L. Brandt, The lift-up effect: the linear mechanism behind transition and turbulence in shear flows, Eur. J. Mech. B Fluids **47**, 80 (2014).
[19] D. Lanzerstorfer and H. C. Kuhlmann, Three-dimensional instability of the flow over a forward-facing step, J. Fluid Mech. **695**, 390 (2012).
[20] K. Chiba, R. Ishida, and K. Nakamura, Mechanism for entry flow instability through a forward-facing step channel, J. Nonnewton. Fluid. Mech. **57**, 271 (1995).
[21] A. Pollard, N. Wakarani, and J. Shawn, Genesis and morphology of erosional shapes associated with turbulent flow over a forward-facing step, in *Coherent Flow Structures in Open Channels*, edited by P. J. Ash-worth, S. J. Bennett, J. L. Best *et al.* (Wiley, Chichester, 1996), pp. 249–265.
[22] H. Stüer, A. Gyr, and W. Kinzelbach, Laminar separation on a forward facing step, Eur. J. Mech. B Fluids **18**, 675 (1999).
[23] D. Wilhelm, C. Härtel, and L. Kleiser, Computational analysis of the two-dimensional-three-dimensional transition in forward-facing step flow, J. Fluid Mech. **489**, 1 (2003).
[24] L. Marino and P. Luchini, Adjoint analysis of the flow over a forward-facing step, Theor. Comput. Fluid Dyn. **23**, 37 (2009).
[25] P. Huerre and P. A. Monkewitz, Local and global instabilities in spatially developing flows, Annu. Rev. Fluid Mech. **22**, 473 (1990).
[26] O. Marxen, M. Lang, U. Rist, O. Levin, and D. S. Henningson, Mechanisms for spatial steady three-dimensional disturbance growth in a non-parallel and separating boundary layer, J. Fluid Mech. **634**, 165 (2009).
[27] A. Bottaro and P. Luchini, Görtler vortices: Are they amenable to local eigenvalue analysis? Eur. J. Mech. B Fluids **18**, 47 (1999).
[28] K. M. Butler and B. F. Farrell, Three-dimensional optimal perturbations in viscous shear flow, Phys. Fluids **4**, 1637 (1992).
[29] S. C. Reddy and D. S. Henningson, Energy growth in viscous channel flows, J. Fluid Mech. **252**, 209 (1993).
[30] P. J. Schmid and D. S. Henningson, *Stability and Transition in Shear Flows* (Springer, New York, 2001).
[31] T. Ellingsen and E. Palm, Stability of linear flow, Phys. Rev. Fluid **18**, 487 (1975).
[32] M. T. Landahl, Wave breakdown and turbulence, SIAM J. Appl. Math. **28**, 735 (1975).
[33] M. T. Landahl, A note on an algebraic instability of inviscid parallel shear flows, J. Fluid Mech. **98**, 243 (1980).

[34] D. S. Henningson, Transient growth with application to bypass transition, in *IUTAM Symposium on Laminar-Turbulent Transition* (Springer Netherlands, Amsterdam, 2006), pp. 15–24.
[35] P. Andersson, M. Berggren, and D. S. Henningson, Optimal disturbances and bypass transition in boundary layers, Phys. Fluids **11**, 134 (1999).
[36] P. Luchini, Reynolds-number-independent instability of the boundary layer over a flat surface: Optimal perturbation, J. Fluid Mech. **404**, 289 (2000).
[37] K. S. Breuer and T. Kuraishi, Transient growth in two- and three-dimensional boundary layers, Phys. Fluids **6**, 1983 (1994).
[38] G. Zoppini, T. Michelis, D. Ragni, and M. Kotsonis, The near wake of discrete roughness elements on swept wings, J. Fluid Mech. **960**, A11 (2023).
[39] P. Corbett and A. Bottaro, Optimal linear growth in swept boundary layers, J. Fluid Mech. **435**, 1 (2001).
[40] D. Tempelmann, A. Hanifi, and D. S. Henningson, Spatial optimal growth in three-dimensional boundary layers, J. Fluid Mech. **646**, 5 (2010).
[41] J. Casacuberta, S. Hickel, and M. Kotsonis, Passive stabilization of crossflow instabilities by a reverse lift-up effect, Phys. Rev. Fluids **9**, 043903 (2024).
[42] S. Albensoeder, H. C. Kuhlmann, and H. J. Rath, Three-dimensional centrifugal-flow instabilities in the lid-driven-cavity problem, Phys. Fluids **13**, 121 (2001).
[43] D. Lanzerstorfer and H. C. Kuhlmann, Global stability of the two-dimensional flow over a backward-facing step, J. Fluid Mech. **693**, 1 (2012).
[44] J.-C. Loiseau, J.-C. Robinet, and E. Leriche, Intermittency and transition to chaos in the cubical lid-driven cavity flow, Fluid Dyn. Res. **48**, 061421 (2016).
[45] F. Picella, J.-C. Loiseau, F. Lusseyran, J.-C. Robinet, S. Cherubini, and L. Pastur, Successive bifurcations in a fully three-dimensional open cavity flow, J. Fluid Mech. **844**, 855 (2018).
[46] J. A. Franco, S. Hein, and E. Valero, Effect of humps and indentations on boundary-layer transition of compressible flows using the AHLNS methodology, in *7th European Conference on Computational Fluid Dynamics (ECFD 7-ECCOMAS)* Glasgow, UK (2018).
[47] J. A. Franco, S. Hein, and E. Valero, On the influence of two-dimensional hump roughness on laminar–turbulent transition, Phys. Fluids **32**, 034102 (2020).
[48] S. H. J. Westerbeek, S. Hulshoff, H. Schuttelaars, and M. Kotsonis, DeHNSSo: The Delft Harmonic Navier-Stokes Solver for nonlinear stability problems with complex geometric features, Comput. Phys. Commun. **302**, 109250 (2024).
[49] R. S. Lin and H. L. Reed, Effect of curvature on stationary crossflow instability of a three-dimensional boundary layer, AIAA J. **31**, 1611 (1993).
[50] P. S. Klebanoff, Effect of free-stream turbulence on the laminar boundary layer, Bull. Am. Phys. Soc. **10** (1971).
[51] J. M. Kendall, Experimental study of disturbances produced in a pre-transitional laminar boundary layer by weak free-stream turbulence, AIAA Paper 85-1695 (1985).
[52] A. K. J. Westin, A. V. Boiko, B. G. B. Klingmann, V. V. Kozlov, and P. H. Alfredsson, Experiments in a boundary layer subjected to free stream turbulence. Part 1. Boundary layer structure and receptivity, J. Fluid Mech. **281**, 193 (1994).
[53] M. Matsubara and P. H. Alfredsson, Disturbance growth in boundary layers subjected to free-stream turbulence, J. Fluid Mech. **430**, 149 (2001).
[54] R. G. Jacobs and P. A. Durbin, Simulations of bypass transition, J. Fluid Mech. **428**, 185 (2001).
[55] L. Brandt, P. Schlatter, and D. S. Henningson, Transition in boundary layers subject to free-stream turbulence, J. Fluid Mech. **517**, 167 (2004).
[56] T. Herbert, Special Course on Progress in Transition Modelling, AGARD report no. 793 (1993).
[57] T. A. Zaki and P. A. Durbin, Mode interaction and the bypass route to transition, J. Fluid Mech. **531**, 85 (2005).
[58] S. Hickel and N. A. Adams, Implicit LES applied to zero-pressure-gradient and adverse-pressure-gradient boundary-layer turbulence, Int. J. Heat Fluid Flow **29**, 626 (2008).

[59] J. Casacuberta, K. J. Groot, Q. Ye, and S. Hickel, Transitional flow dynamics behind a micro-ramp, Flow Turbul. Combust. **104**, 533 (2020).
[60] F. P. Bertolotti, T. Herbert, and P. R. Spalart, Linear and nonlinear stability of the Blasius boundary layer, J. Fluid Mech. **242**, 441 (1992).
[61] L. M. Mack, Boundary-layer linear stability theory, technical report, California Institute of Technology, Pasadena Jet Propulsion Lab (1984).
[62] H. L. Reed, W. S. Saric, and D. Arnal, Linear stability theory applied to boundary layers, Annu. Rev. Fluid Mech. **28**, 389 (1996).
[63] M. Choudhari and C. Streett, Theoretical prediction of boundary-layer receptivity, AIAA Paper 1994-2223 (1994).
[64] Y. Guo, M. Malik, and C. Chang, A solution adaptive approach for computation of linear waves, AIAA Paper 1997-2072 (1997).
[65] A. Y. Dobrinsky, Ph.D. thesis, Adjoint analysis for receptivity prediction, Rice University, 2003.
[66] S. Westerbeek, J. A. Franco, T. Michelis, S. Hein, and M. Kotsonis, Linear and nonlinear stability analysis of a three-dimensional boundary layer over a hump, AIAA Paper 2023-0678 (2023).
[67] J. A. Franco and S. Hein, Adaptive harmonic linearized Navier-Stokes equations used for boundary-layer instability analysis in the presence of large streamwise gradients, AIAA Paper 2018-1548 (2018).
[68] J. M. Floryan, Görtler instability of boundary layers over concave and convex walls, Phys. Fluids **29**, 2380 (1986).
[69] J. Casacuberta, S. Hickel, K. J. Groot, and M. Kotsonis, Direct numerical simulation of instability and breakdown of swept-wing flow with a forward-facing step (unpublished).
[70] A. Antkowiak and P. Brancher, On vortex rings around vortices: an optimal mechanism, J. Fluid Mech. **578**, 295 (2007).
[71] J. M. Floryan and W. S. Saric, Stability of Görtler vortices in boundary layers, AIAA J. **20**, 316 (1982).
[72] W. S. Saric, Nonparallel stability of boundary-layer flows, Phys. Fluids **18**, 945 (1975).
[73] M. Gaster, On the growth of waves in boundary layers: A non-parallel correction, J. Fluid Mech. **424**, 367 (2000).
[74] L. Böberg and U. Brösa, Onset of turbulence in a pipe, Z. Naturforsch. **43**, 697 (1988).